Journal of Scientific Computing (2021) 86:10
https://doi.org/10.1007/s10915-020-01369-9

Exact Splitting Methods for Kinetic and Schrödinger Equations

Joackim Bernier[1,2,3] · Nicolas Crouseilles[4] · Yingzhe Li[5,6,7]

Received: 27 February 2020 / Revised: 28 September 2020 / Accepted: 12 November 2020 /
Published online: 2 January 2021

Abstract
In (Bernier in Exact splitting methods for semigroups generated by inhomogeneous quadratic differential operators. arXiv:1912.13219, (2019)), some exact splittings are proposed for inhomogeneous quadratic differential equations including, for example, transport equations, Fokker–Planck equations, and Schrödinger type equations with an angular momentum rotation term. In this work, these exact splittings are used combined with pseudo-spectral methods in space. High accuracy and efficiency of exact splitting methods are illustrated and comparison are performed with the numerical methods in literature. We show that our methods can be used to improve significantly some classical splitting methods for some nonlinear or non-quadratic equations.

Keywords Exact splitting · Transport equations · Kinetic equations · Schrödinger equations

1 Introduction

Operator splitting methods have gained a lot of attention in recent years to numerically solve partial differential equations, as the subsystems obtained are usually easier to solve and even can be solved exactly, which allows a keen reduction of the computational cost and the derivation of high order time integrators. For a general introduction to splitting methods, we refer to [25,30] and references therein. To obtain high order splitting methods, usually more subsystems in every step are needed to be solved, and proper regularity conditions about the original systems must be assumed. However, there exist some systems for which some specific splitting methods, called exact splittings, can give exact solutions indeed, such as in [2,6,7,13,29].

The author J.B. was supported by the French National Research Agency project NABUCO, grant ANR-17-CE40-0025. The author Y.L. is supported by a scholarship from Academy of Mathematics and Systems Science, Chinese Academy of Sciences. The author N.C. has been supported by the EUROfusion Consortium and has received funding from the Euratom research and training programme 2019–2020 under Grant Agreement No. 633053. The views and opinions expressed herein do not necessarily reflect those of the European Commission.

✉ Joackim Bernier
joackim.bernier@univ-nantes.fr

Extended author information available on the last page of the article

Exact splittings are special splitting methods that can give exact solutions for the original systems. Usually, exact splittings are only available for very simple cases (for example when the operators involved commute). In [12], exact splittings are obtained for a large class of PDEs, namely inhomogeneous quadratic differential equations (see Definition 1 below). In this framework, each subsystem can be solved accurately and efficiently by pseudo-spectral methods or pointwise multiplications. Exact splittings are important and useful for the studies of PDEs theoretically and numerically. They can be of great interest at the theoretical level since they can decompose the original complicated evolution operators into several simpler operators, which gives a way to analyze the properties for the original systems (see [1]). On the numerical side, since the exact splittings we propose can be combined with highly accurate space discretization methods (spectral methods for instance), the resulting fully discrete methods are very accurate and efficient and turn out to be very useful to study the long time behaviors of the original systems.

In this work, our goal is to construct, implement and test in practice the efficiency and accuracy of the exact splitting methods proposed for inhomogeneous quadratic differential equations in [12] on different configurations. Note that even if exact splittings are proposed only for inhomogeneous quadratic differential equations, they can be used to derive new efficient methods for non-quadratic equations by using composition techniques such as Strang splitting. Indeed, equations can be simply split into quadratic parts and non-quadratic parts. First, we will focus on high dimensional transport equations for which efficient exact splittings can be derived from the exact splittings of the underlying linear ordinary differential equations. We compare exact splittings with standard methods from the literature, namely operator splitting method and direct semi-Lagrangian method (combined with NUFFT interpolation). Second, we will apply the exact splittings to solve Fokker–Planck type equations and illustrate two properties of these systems; first, for Fokker–Planck equation, our exact splittings are able to recover the exponential rate of convergence towards the equilibrium and second, the regularizing effects of Kramer–Fokker–Planck equation is captured by our approach. And last but not least, several applications are proposed in the case of Schrödinger type equations. More precisely, we consider the magnetic Schrödinger equation (see [17,28]) and Gross–Pitaevskii equation with a rotation term (see [3,9,11]) for which we compare our exact splittings with efficient methods from the literature. When non-quadratic terms are included in these models (non quadratic potential or nonlinear terms for instance), it is worth mentioning that the new splittings proposed here have a better efficiency (in terms of accuracy and complexity) than methods from the literature and their accuracy increases when the amplitude of the non-quadratic terms becomes smaller. Both for the Fokker–Planck and Schrödinger type equations the derivations of the exact splittings rely on Fourier integral operators developed by Hörmander in [26], which reduces infinite dimensional systems to corresponding finite dimensional systems.

2 Exact Splittings

In this section, we introduce exact splittings for three kinds of inhomogeneous quadratic differential equations: transport, Fokker–Planck, and quadratic

Schrödinger equations, which were studied theoretically in [12]. We start by introducing what we mean by inhomogeneous quadratic equations and exact splittings.

Inhomogeneous quadratic partial differential equations can be written as

$$\begin{cases} \partial_t u(\mathbf{x},t) = -p^w u(\mathbf{x},t), \ t \geq 0, \ \mathbf{x} \in \mathbb{R}^n \\ u(0,\mathbf{x}) \quad = u_0(\mathbf{x}), \qquad\quad \mathbf{x} \in \mathbb{R}^n \end{cases} \tag{1}$$

where $n \geq 1$, $u_0 \in L^2(\mathbb{R}^n)$ and p^w is an inhomogeneous quadratic differential operator acting on $L^2(\mathbb{R}^n)$. When the solution at time t of this equation is well defined, it is denoted, as usual, by $e^{-tp^w}u_0$. This operator p^w is the *Weyl quantization* of a polynomial function (called *symbol*) p on $\mathbb{C}^{2n}$ of degree 2 or less. Usually this quantization is defined through an oscillatory integral (see e.g. Sect. 18.5 in [27] or Chapter 1 in [33]). Nevertheless, since we only deal with inhomogeneous quadratic differential operators, it can be defined much more elementarily. Indeed, in this context, one can write the polynomial function p as

$$p(X) = {}^tXQX + {}^tYX + c, \tag{2}$$

where ${}^t\cdot$ denotes the transposition, $X = ({}^t\mathbf{x}, {}^t\boldsymbol{\xi}) = {}^t(x_1, \ldots, x_n, \xi_1, \ldots, \xi_n)$, Q is a symmetric matrix of size $2n$ with complex coefficients, $Y \in \mathbb{C}^{2n}$ is a vector and $c \in \mathbb{C}$ is a constant. The associated differential operator p^w then writes

$$p^w = {}^t\begin{pmatrix} \mathbf{x} \\ -i\nabla \end{pmatrix} Q \begin{pmatrix} \mathbf{x} \\ -i\nabla \end{pmatrix} + {}^tY \begin{pmatrix} \mathbf{x} \\ -i\nabla \end{pmatrix} + c.$$

For $(-p^w)$ whose real part is bounded by below on $\mathbb{R}^{2n}$, it generates a strongly continuous semigroup on $L^2(\mathbb{R}^n)$ (see e.g. [26]). In [12], one of the authors proved that that e^{-p^w} can be split *exactly* into simple semigroups. As we shall see below, there are several examples which enter in this framework and for which the solutions can be split into operators which are easy to compute. In the following definition, we define what we mean by exact splittings.

Definition 1 An operator acting on $L^2(\mathbb{R}^n)$ can be *computed by an exact splitting* if it can be factorized as a product of operators of the form

$$e^{\alpha\partial_{x_j}}, \ e^{i\alpha x_j}, \ e^{ia(\nabla)}, \ e^{ia(\mathbf{x})}, \ e^{\alpha x_k\partial_{x_j}}, \ e^{-b(\mathbf{x})}, \ e^{b(\nabla)}, \ e^{\gamma} \tag{3}$$

with $\alpha \in \mathbb{R}, \gamma \in \mathbb{C}, a, b : \mathbb{R}^n \to \mathbb{R}$ are some real quadratic forms, b is nonnegative and $j, k \in [\![1, n]\!]$ and $k \neq j$. As usual, $a(\nabla)$ (resp. $b(\nabla)$) denotes the Fourier multiplier associated with $-a(\xi)$ (resp. $-b(\xi)$), i.e. $a(\nabla) = (-a(\xi))^w$.

From the definition 1 of exact splittings, we can see that every subsystem in (3) can be solved exactly in time at least in Fourier variables and as such can be solved efficiently and accurately by pseudo-spectral methods or pointwise multiplications. The resulting fully discretized method will benefit from the spectral accuracy in space so that the error will be negligible in practice.

Below we detail the way we compute the solutions of (1) using pseudo-spectral methods. First, note that, given a factorization of an operator as a product of elementary operators of the form (3), there is a natural and minimal factorization of this operator as product of partial Fourier transforms, inverse partial Fourier transforms and multipliers (i.e. operators associated with a multiplication by a function). So, as usual, we just discretize the partial Fourier transforms, their inverts and the multipliers.

The whole space is truncated and we consider an approximation of the solution on a large box $[-R_1, R_1] \times \cdots \times [-R_n, R_n]$. We discretize the box as a product of grids $\mathbb{G}_1 \times \cdots \times \mathbb{G}_n$ where each grid $\mathbb{G}_j$ has N_j points and is of the form

$$\mathbb{G}_j = h_j[\![-\left\lfloor \frac{N_j - 1}{2} \right\rfloor, \left\lfloor \frac{N_j}{2} \right\rfloor]\!] \tag{4}$$

where $h_j = 2R_j/N_j$ is its cell-size. Associated with such a grid, its dual, denoted by $\widehat{\mathbb{G}_j}$ is

$$\widehat{\mathbb{G}_j} = \eta_j [\![-\left\lfloor \frac{N_j - 1}{2} \right\rfloor, \left\lfloor \frac{N_j}{2} \right\rfloor]\!]$$

where $\eta_j = \pi/R_j$. In this paper, the variable implicitly naturally associated with $\mathbb{G}_j$ (resp. $\widehat{\mathbb{G}_j}$) is denoted g_j (resp. ω_j).

If $\mathcal{L}$ is a product of $(j-1)$ grids (and duals of grids) and $\mathcal{R}$ is a product of $(n-j)$ grids (and duals of grids) then the *discrete* j^{st} *partial Fourier transform* on $\mathcal{L} \times \mathbb{G}_j \times \mathcal{R}$ is defined by

$$\mathcal{F}_j : \begin{cases} \mathcal{L} \times \mathbb{G}_j \times \mathcal{R} \to & \mathbb{C}^{\mathcal{L} \times \widehat{\mathbb{G}_j} \times \mathcal{R}} \\ \psi \qquad\quad \mapsto & \left(h_j \sum_{g_j \in \mathbb{G}_j} \psi_{r, g_j, \ell} e^{-i g_j \omega_j} \right)_{(r, \omega_j, \ell)}. \end{cases}$$

The discrete partial inverse Fourier transforms are defined similarly and are the inverses of the discrete inverse Fourier transforms

$$\mathcal{F}_j^{-1} : \begin{cases} \mathcal{L} \times \widehat{\mathbb{G}_j} \times \mathcal{R} \to & \mathbb{C}^{\mathcal{L} \times \mathbb{G}_j \times \mathcal{R}} \\ \psi \qquad\quad \mapsto & \left(\frac{\eta_j}{2\pi} \sum_{\omega_j \in \widehat{\mathbb{G}_j}} \psi_{r, \omega_j, \ell} e^{i g_j \omega_j} \right)_{(r, g_j, \ell)}. \end{cases}$$

Note that these discrete transforms can be computed efficiently using Fast Fourier Transforms. Finally, the multipliers are naturally discretized through pointwise multiplications. An explicit example is provided in Algorithm 2 for Schrödinger equations.

3 Application to Transport Equations

In this section, we introduce the exact splittings for constant coefficients transport equations. The transport equation we consider here is

$$\partial_t f(\mathbf{x}, t) = (M\mathbf{x}) \cdot \nabla f(\mathbf{x}, t), \quad \mathbf{x} \in \mathbb{R}^n, \ n \geq 1, \ f(\mathbf{x}, t = 0) = f_0(\mathbf{x}), \tag{5}$$

where M is a real square matrix of size $n \geq 1$ such that

$$\begin{cases} \forall i, & M_{i,i} = 0, \\ \exists i, \forall j \neq i, & M_{j,i} \neq 0, \end{cases} \tag{6}$$

and the corresponding symbol of (5) is $p(X) = -i(M\mathbf{x}) \cdot \boldsymbol{\xi}$ according to the notation (2).

Even if the solution of (5) can be computed from the initial condition as $f(\mathbf{x}, t) = f_0(e^{tM}\mathbf{x})$, efficient numerical methods are required when the initial data is only known on a mesh or when (5) is a part of more complex models. Below, we start by giving some details of the time (exact) splittings before illustrating the efficiency with numerical results.

3.1 Presentation of the Exact Splittings

In this part, we construct an exact splitting for (5). Let us start with a simple example for $n = 2$ and $M = \begin{pmatrix} 0 & 1 \\ -1 & 0 \end{pmatrix}$, e^{tM} becomes a two dimensional rotation matrix, which can be expressed as the product of three shear matrices (see [13])

$$e^{tM} = \begin{pmatrix} 1 & \tan(t/2) \\ 0 & 1 \end{pmatrix} \begin{pmatrix} 1 & 0 \\ -\sin t & 1 \end{pmatrix} \begin{pmatrix} 1 & \tan(t/2) \\ 0 & 1 \end{pmatrix}. \tag{7}$$

As a consequence, the computation of f can be done by solving three one dimensional linear equations (in x_1, x_2, and x_1 directions successively), i.e.,

$$f_0(\mathbf{x}) \overset{\tan(t/2)}{\longrightarrow} f_0(x_1 + \tan(t/2)x_2, x_2) \overset{-\sin(t)}{\longrightarrow} f_0(x_1 + \tan(t/2)(x_2 - \sin(t)x_1), x_2 - \sin(t)x_1) \overset{\tan(t/2)}{\longrightarrow} f(\mathbf{x}, t). \tag{8}$$

Formula (7) has been used in the computation of Vlasov–Maxwell equations to improve efficiency and accuracy by avoiding high dimensional reconstructions in [2,13].

For the case $n = 3$ and M is skew symmetric, similar formula of expressing the rotation matrix e^{tM} as the product of 4 shear matrices is proposed in [18,34]. To generalize this formula to transport equations in arbitrary dimension, we have the following result proved in [12].

Proposition 1 *Let M be a real square matrix of size $n \geq 1$ satisfying condition (6) and $i \in \{1, \ldots, n\}$, then there exist $t_0 > 0$ and an analytic function $(y^{(\ell)}, (y^{(k)})_{k=1,\ldots,n;k\neq i}, y^{(r)}) : (-t_0, t_0) \to \mathbb{R}^{n\times(n+1)}$ satisfying*

$$\begin{cases} y_i^{(\ell)} = y_i^{(r)} = 0 \\ \forall k \neq i,\ y_k^{(k)} = 0 \end{cases} \tag{9}$$

such that for all $t \in (-t_0, t_0)$ we have

$$e^{tM\boldsymbol{x}\cdot\nabla} = e^{t(y^{(\ell)}(t)\cdot\mathbf{x})\partial_{x_i}} \left(\prod_{k\neq i} e^{t(y^{(k)}(t)\cdot\boldsymbol{x})\partial_{x_k}} \right) e^{t(y^{(r)}(t)\cdot\mathbf{x})\partial_{x_i}}. \tag{10}$$

Remark 1 Proposition 1 not only enables to recover some results from the literature (in particular when M is skew symmetric) but also it claims that n dimensional linear equations of the form (5) can be split into $(n + 1)$ one dimensional linear equations which can be solved very efficiently by means of pseudo-spectral methods or semi-Lagrangian methods. In particular, this turns out to be much more efficient than standard Strang splitting which would require $2(n - 1) + 1$ one dimensional linear equations to solve. Let us also recall that Strang splittings are second order accurate whereas the splittings proposed in Proposition 1 are *exact* in time.

Remark 2 Let us remark that when every non-diagonal element of M is not zero, $n!$ different exact splittings (10) can be constructed, which is the number of permutations of set $\{1, 2, \cdots, n\}$.

Remark 3 Another alternative to solve (5) would be the direct n-dimensional semi-Lagrangian method. However, this approach brings huge computational cost at the interpolation stage.

3.2 Practical Construction of the Exact Splitting

Following Proposition 2.1 in [12], we write a code from Algorithm 1 to compute the coefficients $y^{(\ell)}$, $y^{(r)}$, $y^{(k)}(k \neq i)$ arising in the exact splitting (10). For the sake of simplicity, we present the pseudo-code to construct the following splitting

$$e^{tM\mathbf{x}\cdot\nabla} = e^{t(y^{(\ell)}(t)\cdot\mathbf{x})\partial_{x_1}} \left(e^{t(y^{(2)}(t)\cdot\mathbf{x})\partial_{x_2}} \ldots e^{t(y^{(n)}(t)\cdot\mathbf{x})\partial_{x_n}} \right) e^{t(y^{(r)}(t)\cdot\mathbf{x})\partial_{x_1}}.$$

Algorithm 1 Pseudo-code for (10)

Input:

$B = {}^{t}M$, denote $B_{\star,j}$ the jth column of B,

I_n the identity matrix of size n, e_j the jth element of the canonical basis of $\mathbb{R}^n$,

t the time step and $N \in \mathbb{N}^\star$

Initialize $y^{(m)}, y^{(\ell)}, y^{(r)}, y^{(j)}$ for $j = 2, \dots, n$.

for $k = 1$ to N **do**

$P = (I_n + t\, y_k^{(\ell)} \otimes e_1)\Big(\Pi_{j=2}^{n}(I_n + t\, y_k^{(j)} \otimes e_j)\Big)(I_n + t\, y_k^{(r)} \otimes e_1)$,

$g = 1/t \ \log(P)$,

$\Pi^\tau = [B, \mathbf{v} \otimes e_1]$ with $\mathbf{v} \in \mathbb{R}^n$ s.t. $\mathbf{v}_1 = 0$ and $\mathbf{v}_j = -g_{j,j}/B_{1,j}$ for $j = 2, \dots, n$,

$\Pi^b = g - \Pi^\tau$,

$y_{k+1}^{(m)} = y_k^{(m)} + B_{\star,1} - \Pi^b_{\star,1}$,

$y_{k+1}^{(j)} = y_k^{(j)} + B_{\star,j} - \Pi^b_{\star,j}$, for $j = 2, \cdots, n$,

$y_{k+1}^{(r)} = y_k^{(r)} - \frac{1}{t}\,\mathbf{v}$,

$y_{k+1}^{(\ell)} = y_{k+1}^{(m)} - y_{k+1}^{(r)}$,

end for

Output: $y^{(r)} = y_{N+1}^{(r)}, y^{(l)} = y_{N+1}^{(\ell)}, y^{(j)} = y_{N+1}^{(j)}, j = 2, \cdots, n$.

The iteration number N is chosen large enough to ensure the convergence of the algorithm.

3.3 Numerical Results

Exact splittings are used to solve 3D and 4D transport equations, and compared with the usual Strang splittings and Semi-Lagrangian methods combined with NUFFT in space. We are interested in the numerical approximation of

$$\partial_t f(\mathbf{x}, t) = (M\mathbf{x}) \cdot \nabla f(\mathbf{x}, t), \quad f(\mathbf{x}, t = 0) = f_0(\mathbf{x}), \quad \mathbf{x} \in \mathbb{R}^n, \tag{11}$$

for $n = 3, 4$. For numerical reasons, the domain will be truncated to $[-R, R]^n$ and we will consider N points per direction so that the mesh size is $h = 2R/N$. The grid, defined as usual through (4), is denoted $\mathbb{G}^n$. We shall denote f_g^n by an approximation of the exact solution of (11) with $g \in \mathbb{G}^n$, and $\Delta t > 0$ is the time step. We also define the L^2 error between the numerical solution and the exact one as

$$\sqrt{h^n \sum_{g \in \mathbb{G}^n} |f_g^n - f(n\Delta t, g)|^2}. \tag{12}$$

3D transport equation

We consider (11) in the case $n = 3$ with

$$M = \begin{pmatrix} 0 & -0.36 & -0.679 \\ 0.36 & 0 & -0.758 \\ 0.679 & 0.758 & 0 \end{pmatrix}.$$

The domain is defined by $R = 2$ and initial value is chosen as follows

$$f_0(\mathbf{x}) = \frac{1}{2(\pi\beta)^2}\Big(e^{-(x_1-0.3)^2/\beta} + e^{-(x_1+0.3)^2/\beta}\Big)e^{-x_2^2/\beta}e^{-x_3^2/\beta},$$

with $\beta = 0.06$. The following three numerical methods are used to solve the three dimensional transport equation

– NUFFT: direct 3D Semi-Lagrangian method combined with interpolation by NUFFT; this method is exact in time.
– Strang: Strang directional splitting method combined with Fourier pseudo-spectral method; this method is second order accurate in time.
– ESR: Exact splitting (10) combined with Fourier pseudo-spectral method; this method is exact in time.

Let us detail the coefficients used for ESR. From Prop. 1 (with $i = 3$), we have

$$e^{\Delta t M\mathbf{x}\cdot\nabla} = e^{\Delta t(y^{(\ell)}\cdot\mathbf{x})\partial_{x_3}} e^{\Delta t(y^{(1)}\cdot\mathbf{x})\partial_{x_1}} e^{\Delta t(y^{(2)}\cdot\mathbf{x})\partial_{x_2}} e^{\Delta t(y^{(r)}\cdot\mathbf{x})\partial_{x_3}},$$

where the coefficients are as follows when $\Delta t = 0.3$

$$y^{(\ell)} \simeq \begin{pmatrix} 0.467187759219503 \\ 0.257781732992119 \\ 0 \end{pmatrix}, \quad y^{(1)} \simeq \begin{pmatrix} 0 \\ -0.381811510002637 \\ -0.626618917055694 \end{pmatrix},$$

and

$$y^{(2)} \simeq \begin{pmatrix} 0.386696405646122 \\ 0 \\ -0.708474220370764 \end{pmatrix}, \quad y^{(r)} \simeq \begin{pmatrix} 0.205015116583865 \\ 0.492630313928284 \\ 0 \end{pmatrix}.$$

First, the time evolution of the L^2 error (defined by (12)) is plotted in Fig. 1 for Strang and ESR for $N = 64$ and $\Delta t = 0.3$. As expected, we observe that the error from ESR is close to the level of 10^{-11} whereas the error from Strang is much larger. We can also see that the error from Strang has an almost periodic behavior (similar to what has been observed in 2D case in [13]). As in [13], this phenomena is well explained by its backward error analysis. In the Sect. 1 of the Appendix, we prove that it is associated with the transport equation of a rotation (up to a near identity map) whose pulsation coincides with that of e^{tM} up to a correction of order Δt^2. We also compare in Fig. 1 the CPU time of the two methods and the NUFFT method (which also gives error close to machine precision) by running them for 100 steps. We can observe that ESR is the most efficient. Indeed, for each time step, 5 one dimensional transport equations are needed for Strang splitting, whereas ESR only has 4 one dimensional transport equations to solve. Moreover, the NUFFT method is the most expensive, even if NUFFT and ESR have the same complexity $\mathcal{O}(N^3 \log(N))$. Let us mention that parallelization can be developed to improve the efficiency of splitting methods like ESR (see [13,19]).

4D transport equation

We consider now the case $n = 4$ where the matrix M in (5) is given by

$$M = \begin{pmatrix} 0 & 1 & -1.5 & -3 \\ -1 & 0 & 2 & 1 \\ 1.5 & -2 & 0 & 0 \\ 3 & -1 & 0 & 0 \end{pmatrix}.$$

The domain is defined by $R = 5$ and the initial value is

$$f_0(\mathbf{x}) = \left(\frac{2}{\pi}\right)^4 e^{-|\mathbf{x}|^2}. \tag{13}$$

Since the direct 4D semi-Lagrangian method would be too costly, we compare here the Strang directional splitting and the new method ESR. From Proposition 1, we define the

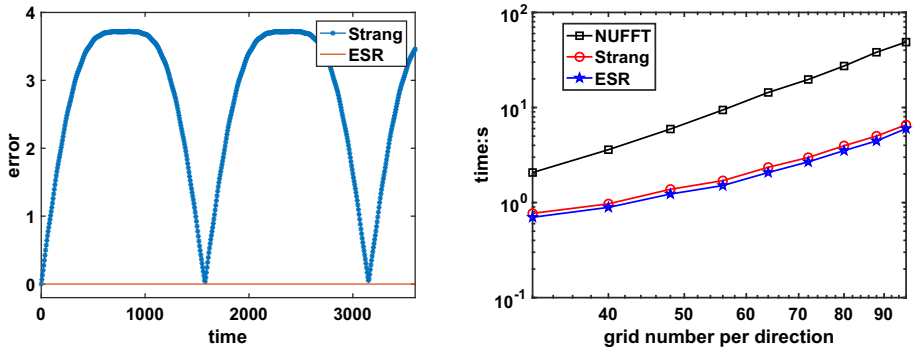

Fig. 1 **a** Time evolution of L^2 error (semi-$\log_{10}$ scale) for NUFFT, ESR, and Strang for 3D transport problem with grids $64 \times 64 \times 64$ and step size $\Delta t = 0.3$; **b** CPU time for NUFFT, ESR and Strang of running 100 steps

ESR method by (here we have chosen $i = 2$)

$$e^{\Delta t M \mathbf{x}\cdot\nabla} = e^{\Delta t (y^{(\ell)}\cdot\mathbf{x})\partial_{x_2}} \left(e^{\Delta t (y^{(1)}\cdot\mathbf{x})\partial_{x_1}} e^{\Delta t (y^{(3)}\cdot\mathbf{x})\partial_{x_3}} e^{\Delta t (y^{(4)}\cdot\mathbf{x})\partial_{x_4}} \right) e^{\Delta t (y^{(r)}\cdot\mathbf{x})\partial_{x_2}},$$

whose coefficients are (when $\Delta t = 0.05$)

$$y^{(\ell)} \simeq {}^{\mathrm{t}}(-5.344642460486645,\, 0,\, 0.823467853756413,\, -2.992867555994520),$$
$$y^{(r)} \simeq {}^{\mathrm{t}}(3.737426150781880,\, 0,\, 1.523124853600163,\, 4.681057037906191),$$
$$y^{(1)} \simeq {}^{\mathrm{t}}(0,\, 1.142288588772368,\, -1.484580777109155,\, -2.786376511283418),$$
$$y^{(3)} \simeq {}^{\mathrm{t}}(1.015044786749623,\, -2.011875030994669,\, 0,\, -0.314761305209573),$$
$$y^{(4)} \simeq {}^{\mathrm{t}}(2.758340963158925,\, -1.064751317849253,\, !\,0.082700298557278,\, 0).$$

The space grid has $N = 47$ points per direction and the final computation time is $t = 100$ for the two methods (Strang and ESR). Contour plots of $f(t, x_1, x_2, x_3 = -0.9574, x_4 = -0.9574)$ at $t = 100$ by ESR, Strang method are presented in Fig. 2a, b. Compared with the exact solution in Fig. 2c, we can observe that the Strang method has larger error which is partly due to the wrong angular velocity. Moreover, in Fig. 2d, the time evolutions of the L^2 error defined in (12) are plotted for the Strang method (10^{-2}) and ESR method (10^{-11}). Let us remark that other than pseudo-spectral method, alternative reconstruction methods can also be chosen such as high order interpolation methods (see [16]). Regarding the complexity, only $n+1 = 5$ shears are required in the exact splitting for each time step whereas $2n-1 = 7$ shears are needed for the Strang splitting.

4 Application to Fokker–Planck Equations

In this section, we are interested in Fokker–Planck type equations which can be used to describe particle systems (in plasma physics or astrophysics). The unknown is a distribution function of particles $f(t, x, v) \in \mathbb{R}^+$ with time $t \geq 0$, space $x \in \mathbb{R}$, and velocity $v \in \mathbb{R}$. We will focus on two examples which both contain a free transport part in x and an operator (related to collisional terms) which only acts on the v direction. The first example is the Kramer–Fokker–Planck equation (see [20,22,23] for some mathematical and numerical

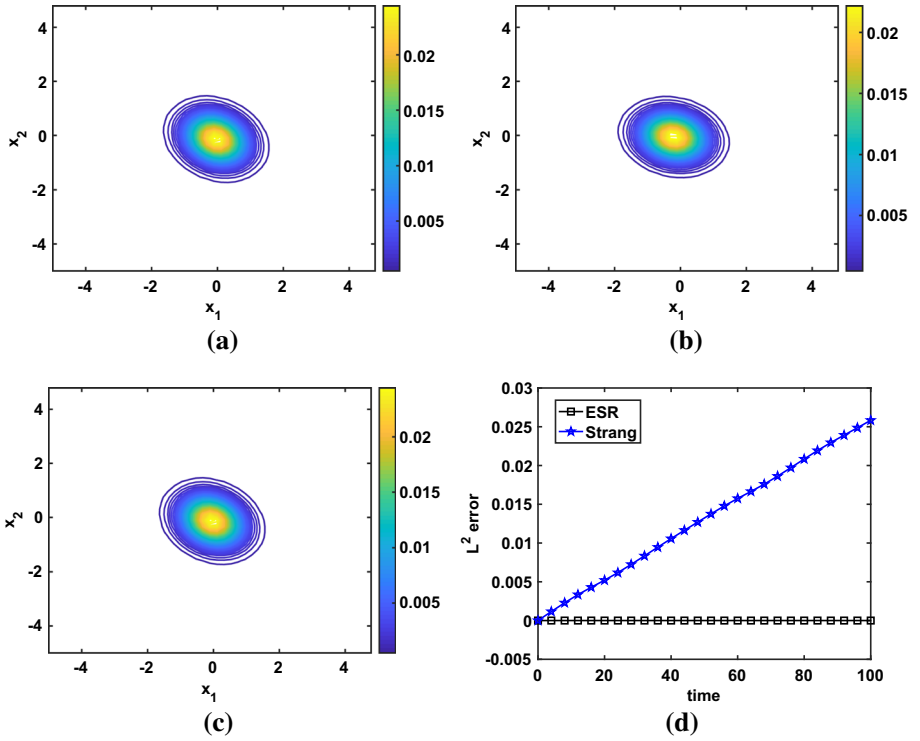

Fig. 2 **a** Contour plots of $f(t = 30, x_1, x_2, -0.9574, -0.9574)$ computed by **a** ESR and **b** Strang method; **c** Contour plots of exact $f(t = 30, x_1, x_2, -0.9574, -0.9574)$; **d** Time evolution of L^2 solution error

aspects)

$$\partial_t f + v^2 f - \partial_v^2 f + v\partial_x f = 0, \quad f(t = 0, x, v) = f_0(x, v). \tag{KFP}$$

The second example is the Fokker–Planck equation (see [20,22,24] for some mathematical and numerical aspects)

$$\partial_t f + v\partial_x f - \partial_v^2 f - \partial_v(vf) = 0, \quad f(t = 0, x, v) = f_0(x, v). \tag{FP}$$

For these two examples which enter in the class of inhomogeneous quadratic equations, exact splittings will be recalled from [12] and numerical results will be given.

4.1 Presentation of the Exact Splittings

For the Kramer–Fokker–Planck (KFP) equation, the symbol is $p(x, v, \xi, \eta) = v^2 + \eta^2 + iv\xi$, and the symbol is $p(x, v, \xi, \eta) = iv\xi + \eta^2 - iv\eta - \frac{1}{2}$ for the Fokker–Planck (FP) equation, where ξ (resp. η) denotes the Fourier variable of x (resp. v). We can see that for both cases, the symbols are polynomial functions of degree 2 and according to [12], the solutions can be split exactly into simple flows. More precisely, for KFP, we have the following exact splitting formula

$$\forall t \geq 0, \ e^{-t(v^2 - \partial_v^2 + v\partial_x)} = e^{-\frac{1}{2}\tanh(t)\, v^2} e^{\nabla\cdot(A_t^{\mathrm{KFP}}\nabla)} e^{-\tanh(t)\, v\partial_x} e^{-\frac{1}{2}\tanh(t)\, v^2}, \tag{14}$$

with $\nabla = (\partial_x, \partial_v)$ and where A_t is the following nonnegative matrix defined by

$$A_t^{\mathrm{KFP}} = \frac{1}{2}\begin{pmatrix} \frac{1}{2}\left(t - \tanh(t)(1-\sinh^2(t))\right) & \sinh^2(t) \\ \sinh^2(t) & \sinh(2t) \end{pmatrix}. \tag{15}$$

For FP, we have the exact splitting formula

$$e^{-t(v\partial_x - \partial_v^2 - \partial_v v)} = e^{t/2} e^{-(e^t-1)v\partial_x} e^{\nabla\cdot(A_t^{\mathrm{FP}}\nabla)} e^{i\alpha_t\partial_v^2} e^{-i\beta_t v^2} e^{-i\beta_t\partial_v^2} e^{i\alpha_t v^2}, \tag{16}$$

where $\alpha_t = \frac{1}{2}\sqrt{(1-e^{-t})e^{-t}}$, $\beta_t = \frac{1}{2}\sqrt{e^t - 1}$, and A_t^{FP} is the following positive matrix (see [1]) defined by

$$A_t^{\mathrm{FP}} = \frac{1}{2}\begin{pmatrix} e^{2t} + 2t + 3 - 4e^t & -4\sinh^2(t/2) \\ -4\sinh^2(t/2) & 1 - e^{-2t} \end{pmatrix}.$$

Below, we detail a bit the link between exact splittings for PDEs and corresponding finite dimensional Hamiltonian systems on the example of KFP. Following [12], the exact splitting (14) is equivalent to the following equality between matrices

$$e^{-2itJQ} = e^{-2itJQ_1} e^{-2itJQ_2} e^{-2itJQ_3} e^{-2itJQ_1}, \tag{17}$$

where J is the symplectic 4×4 matrix, $Q, Q_i \in \mathrm{S}_4(\mathbb{C})$ $(i = 1,2,3)$ are the matrices corresponding to the quadratic forms q, q_i $(i = 1,2,3)$ defining the operators involved in the exact splitting (14). Indeed, the quadratic form q associated to the quadratic operator $q^w := v^2 - \partial_v^2 + v\partial_x$ is $q(X) = {}^tXQX$ with $X = (x, v, \xi, \eta)$ and Q is

$$Q = \begin{pmatrix} 0 & 0 & 0 & 0 \\ 0 & 1 & i/2 & 0 \\ 0 & i/2 & 0 & 0 \\ 0 & 0 & 0 & 1 \end{pmatrix}.$$

Let us define the other quadratic forms involved in (14): $q_1(X) = \frac{\tanh(t)}{t}v^2 = {}^tXQ_1X$, $q_2(X) = {}^tXQ_2X$, $q_3 = i\frac{\tanh(t)}{t}v\xi = {}^tXQ_3X$ where

$$Q_1 = \frac{\tanh(t)}{t}\begin{pmatrix} 0&0&0&0 \\ 0&1&0&0 \\ 0&0&0&0 \\ 0&0&0&0 \end{pmatrix},\quad Q_2 = \frac{1}{t}\begin{pmatrix} \mathbf{0}_2 & \mathbf{0}_2 \\ \mathbf{0}_2 & A_t^{KFP} \end{pmatrix},\quad Q_3 = \frac{\tanh(t)}{t}\begin{pmatrix} 0&0&0&0 \\ 0&0&i/2&0 \\ 0&i/2&0&0 \\ 0&0&0&0 \end{pmatrix},$$

$\mathbf{0}_2$ is the zero 2x2 matrix and A_t^{KFP} is given by (15).

4.2 Numerical Results

In this section, numerical simulations are performed using the above exact splittings to illustrate the exponential decay to equilibrium property and regularizing effects. Let us remark that since the Fokker–Planck and Krammer–Fokker–Planck operators are homogeneous with respect to the space variable x, we do not have to consider localized functions and thus consider periodic functions in this direction. The domain is truncated to $[-R_1, R_1]\times[-R_2, R_2]$ and the number of uniform grids is N_1 (resp. N_2) in x-direction (resp. the v-direction).

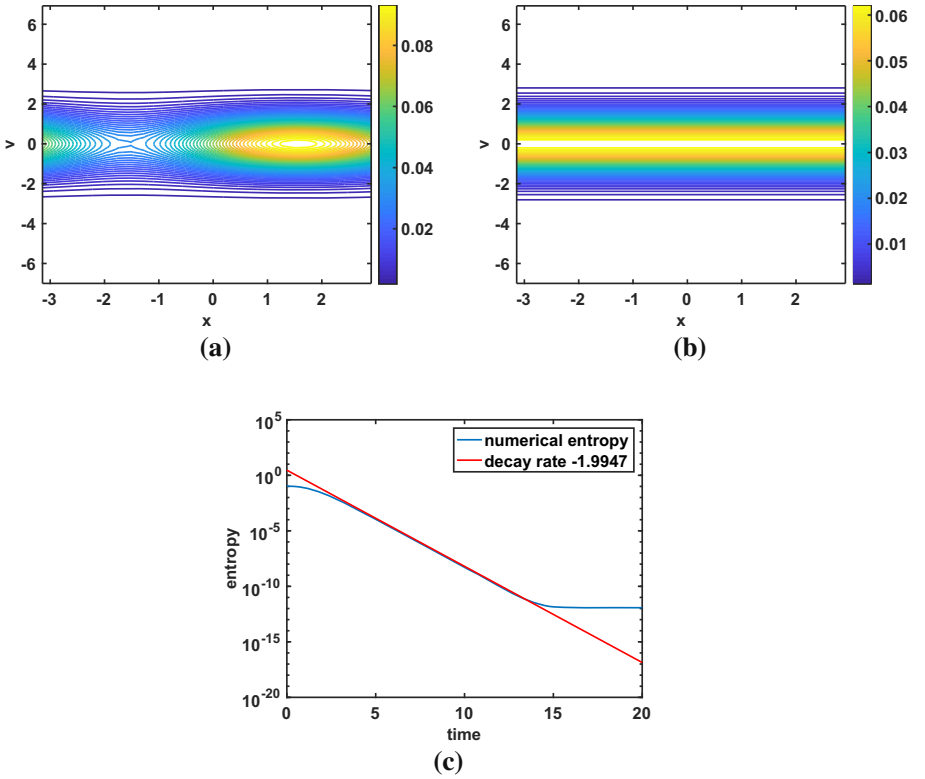

Fig. 3 **a** Initial distribution function $f(t = 0, x, v)$; **b** distribution function at $t = 20$: $f(t = 20, x, v)$; (c) time evolution of the entropy given by (18)

Fokker–Planck equation

For the FP equation, we aim at checking an important property that the solution converges to the equilibrium state exponentially with time (see [20]). The domain is taken as $R_1 = \pi$ and $R_2 = 7$ (so that $(x, v) \in [-\pi, \pi] \times [-7, 7]$). The initial function is

$$f_0(x, v) = \frac{1}{\sqrt{2\pi}} \exp(-v^2/2) \left(1 + 0.5 \sin(x) \cos(\frac{\pi}{7} v)\right).$$

We are interested in the time evolution of the entropy which is defined by

$$\mathcal{F}(t) = \int_0^L \int_{-\infty}^{\infty} \frac{(f(t, x, v) - \mu(v))^2}{\mu(v)} \mathrm{d}v\mathrm{d}x, \tag{18}$$

with $\mu(v) = \frac{1}{\sqrt{2\pi}} e^{-\frac{v^2}{2}}$.

The numerical parameters are $N_1 = 27$, $N_2 = 181$, the time step is $\Delta t = 0.1$ and the simulation is ended at $t = 20$. In Fig. 3, the contour plots of distribution function are plotted at the initial and the ending time and we can observe the relaxation towards the Maxwellian profile. This is more quantitatively shown in Fig. 3c where the time history of entropy (18) is plotted. Indeed, the exponential decay is clearly observed, the rate is equal to -1.99 (red straight line), which is in good agreement with [20].

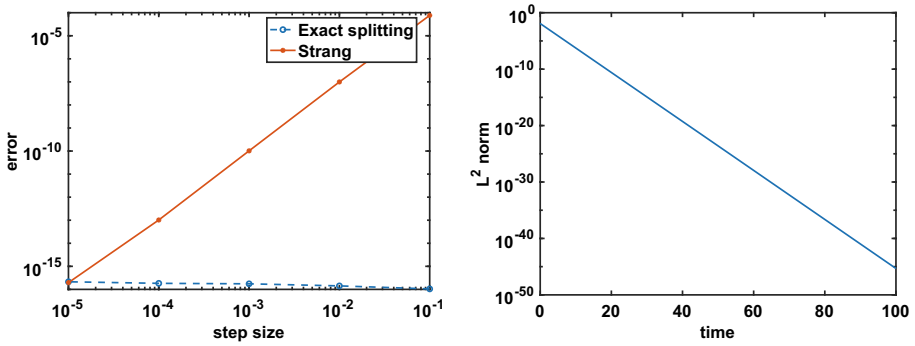

Fig. 4 **a** L^2 error ($\log_{10} - \log_{10}$ scale) of the formula (19) with different time step size Δt; **b** Time evolution of the L^2 norm (in x and v) of f in semi-$\log_{10}$ scale

Kramer–Fokker–Planck equation

Now we apply the exact splitting for the numerical simulation of the KFP equation. The domain is chosen with $R_1 = 4$ and $R_2 = 15$ (so that $(x, v) \in [-4, 4] \times [-15, 15]$). In the following experiments, we consider $N_1 = N_2 = 199$. The initial function is

$$f_0(x, v) = \frac{1}{8\sqrt{2\pi}} e^{-\frac{v^2}{2}}.$$

First, in Fig. 4a, we plot the L^2 norm (in $\log_{10} - \log_{10}$ scale) of the following formula

$$e^{-\Delta t(v^2 - \partial_v^2 + v\partial_x)} f_0(x, v) - e^{-\Delta t/2(v^2 - \partial_v^2 + v\partial_x)} e^{-\Delta t/2(v^2 - \partial_v^2 + v\partial_x)} f_0(x, v) \tag{19}$$

using different time steps. Two different methods are used to compute

$e^{-t(v^2 - \partial_v^2 + v\partial_x)} f_0(x, v)$: the exact splitting (14) and a Strang operator splitting. First, we observe that the exact splitting gives an error at the machine precision level whereas we obtain an error of $\mathcal{O}(\Delta t^3)$ which corresponds the local error of the Strang method and confirms the correct implementation of the algorithms.

Then, we illustrate the regularizing effects property of the evolution operator in KFP [1]. To do so, the initial condition is chosen as random values (discrete L^1 norm is 1) and the step size is $\Delta t = 0.1$. In Fig. 5, the contour plots of distribution function are displayed for different times: $t = 0, 0.2, 1, 100$. We observe that starting from a random initial value, the numerical solution becomes smoother as time increases. Moreover, it can be proved that the solution is exponentially decreasing towards zero with time. This is illustrated in Fig. 4b where we plot the time history of L^2 norm of f (semi-$\log_{10}$ scale).

5 Application to Schrödinger Equations

In this section, we recall and apply exact splitting methods for Schrödinger type equations in [12]: magnetic Schrödinger equations, and rotating Gross-Pitaevskii equations (see [5,9, 11,17,32] for more details on these models).

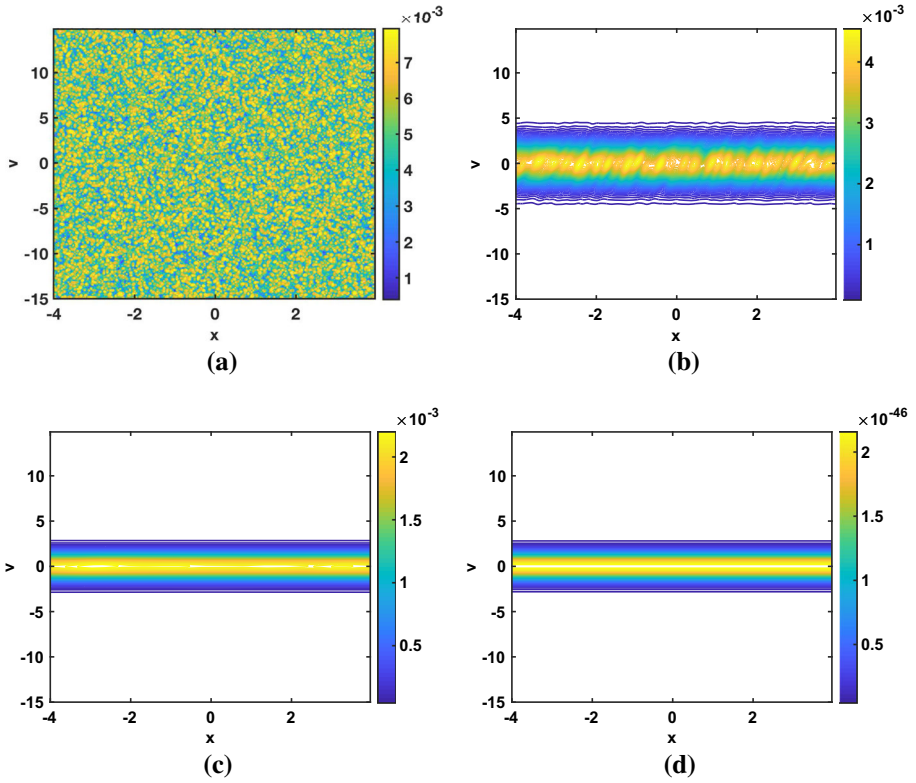

Fig. 5 Time evolution of the distribution function f **a** $t = 0$; **b** $t = 0.2$; **c** $t = 1$; **d** $t = 100$

We consider the following linear Schrödinger equation (with a rotation term and a quadratic external potential) of unknown $\psi(\mathbf{x}, t) \in \mathbb{C}$ with $\mathbf{x} \in \mathbb{R}^n$, $t \in \mathbb{R}_+$

$$i\frac{\partial \psi(\mathbf{x}, t)}{\partial t} = -\frac{1}{2}\Delta\psi(\mathbf{x}, t) - i(B\mathbf{x}) \cdot \nabla\psi(\mathbf{x}, t) + V(\mathbf{x})\psi(\mathbf{x}, t), \quad \psi(\mathbf{x}, t = 0) = \psi_0(\mathbf{x}), \tag{QM}$$

where $n \in \mathbb{N}^*$, $B \in A_n(\mathbb{R})$ is a skew symmetric matrix of size n and $V : \mathbb{R}^n \to \mathbb{R}$ is a quadratic potential. According to the previous framework, this model is an inhomogeneous quadratic PDE, since it can be represented by the following symbol

$$p(X) = i\frac{|\boldsymbol{\xi}|^2}{2} + iB\mathbf{x} \cdot \boldsymbol{\xi} + iV(\mathbf{x}), \quad X = (\mathbf{x}, \boldsymbol{\xi}) \in \mathbb{R}^{2n}. \tag{20}$$

In the sequel, an exact splitting is presented. Then, extensions to nonlinear and non-quadratic Schrödinger equations are discussed. This section will be ended by several numerical results that will be compared to different numerical methods from the literature to illustrate the efficiency of our approach.

5.1 Presentation of the Exact Splitting

We present an exact splitting method for (QM) which has been introduced in [12].

Theorem 1 *There exists some quadratic forms $v_t^{(r)}, a_t$ on $\mathbb{R}^n$, a strictly upper triangular matrix $U_t \in M_n(\mathbb{R})$, a strictly lower triangular matrix $L_t \in M_n(\mathbb{R})$ and a diagonal quadratic form $v_t^{(\ell)}$ on $\mathbb{R}^n$, all depending analytically on $t \in (-t_0, t_0)$ for some $t_0 > 0$, such that for all $t \in (-t_0, t_0)$ we have*

$$e^{it(\Delta/2 - V(\boldsymbol{x})) - tB\boldsymbol{x}\cdot\nabla} = e^{-itv_t^{(\ell)}(\boldsymbol{x})} \left(\prod_{j=1}^{n-1} e^{-t(U_t\boldsymbol{x})_j \partial_{x_j}} \right) e^{ita_t(\nabla)} \left(\prod_{j=2}^{n} e^{-t(L_t\boldsymbol{x})_j \partial_{x_j}} \right) e^{-itv_t^{(r)}(\boldsymbol{x})} \tag{21}$$

where $a_t(\nabla)$ denotes the Fourier multiplier of symbol $-a_t(\boldsymbol{\xi})$ and $(U_t\boldsymbol{x})_j$ (resp. $(L_t\boldsymbol{x})_j$) the j^{st} coordinate of $U_t\mathbf{x}$ (resp. $L_t\boldsymbol{x}$).

Let us detail this splitting to emphasize the fact that due to the triangular structure of the matrices L_t and U_t, only $2n$ FFT calls are required in every step:

- From $e^{-itv_t^{(r)}(\mathbf{x})}$ to $e^{-t(L_t\mathbf{x})_n \partial_{x_n}}$, we need a FFT in x_n direction;
- From $e^{-t(L_t\mathbf{x})_j \partial_{x_j}}$ to $e^{-t(L_t\mathbf{x})_{j-1}\partial_{x_{j-1}}}$, $j \in [\![3, n]\!]$, as L_t is a strictly lower triangular matrix, $(L_t\mathbf{x})_j$ only depends on x_i, $i \in [\![1, j-1]\!]$, then we only need a FFT in x_{j-1} direction.
- From $e^{-t(L_t\mathbf{x})_2\partial_{x_2}}$ to $e^{ita_t(\nabla)}$, we need a FFT in x_1 direction.
- From $e^{ita_t(\nabla)}$ to $e^{-t(U_t\mathbf{x})_{n-1}\partial_{x_{n-1}}}$, we need an inverse FFT in x_n direction;
- From $e^{-t(U_t\mathbf{x})_j\partial_{x_j}}$ to $e^{-t(U_t\mathbf{x})_{j-1}\partial_{x_{j-1}}}$, $j \in [\![2, n-1]\!]$, because U_t is a strictly upper triangular matrix, $(U_t\mathbf{x})_{j-1}$ only depends on x_i, $i \in [\![j, n]\!]$, we only need an inverse FFT in x_j direction.
- From $e^{-t(U_t\mathbf{x})_1\partial_{x_1}}$ to $e^{-itv_t^{(\ell)}(\mathbf{x})}$, we need an inverse FFT in x_1 direction.

To sum up, this new method only needs $2n$ FFT (or inverse FFT) calls in every time step.

Below, we detail a bit the link of exact splittings between the Schrödinger equations and corresponding finite dimensional Hamiltonian systems. Following [12], the exact splitting (21) is equivalent to prove an equality at the level of matrices. Indeed, from Hörmander [26], there exists a morphism between the Hamiltonian flow of the following linear ODE $\dot{X} = -iJ\nabla p(X)$ and e^{-p^w} (up to one sign), where J is the symplectic matrix of size $2n$. So we can check the following exact splitting at the linear ODE level for (21):

$$e^{-2itJQ} = e^{-2itJV^{(\ell)}} \left(\prod_{j=1}^{n-1} e^{-2itJU^{(j)}} \right) e^{-2itJA} \left(\prod_{j=2}^{n} e^{-2itJL^{(j)}} \right) e^{-2itJV^{(r)}}, \tag{22}$$

where $Q, V^{(\ell)}, U^{(j)}, A, L^{(j)}, V^{(r)}$ are symmetric matrices of the quadratic forms (symbols) of the following operators $iv_t^{(\ell)}(\mathbf{x})$, $i(U_t\mathbf{x})_j\partial_{x_j}$, $-iA_t(\nabla)$, $i(L_t\mathbf{x})_j\partial_{x_j}$, $iv_t^{(r)}(\mathbf{x})$ respectively.

5.2 Practical Construction of the Splittings

In this subsection, the iteration method giving the coefficients in the above exact splitting is presented. The proof for Theorem 1 is based on the implicit function theorem which gives a practical way to construct the exact splitting. Indeed, it furnishes an iteration method which is presented below. We refer to [12] for more details.

In this context, the iterative method giving the coefficients of the exact splitting can be made much more explicit. Indeed, identifying a quadratic form with its symmetric matrix, if

the time step size t is small enough, we define, by induction, the following sequences

$$\begin{cases} A_{t,k+1} = A_{t,k} + I_n/2 - \widetilde{A}_{t,k} \\ L_{t,k+1} = L_{t,k} + L - \widetilde{L}_{t,k} \\ U_{t,k+1} = U_{t,k} + U - \widetilde{U}_{t,k} \\ V^{(m)}_{t,k+1} = V^{(m)}_{t,k} + V - \widetilde{V}^{(m)}_{t,k} + \frac{t}{2}[D_{t,k}, B] + \frac{t^2}{2} D^2_{t,k} \end{cases}$$

where $(A_{t,0}, L_{t,0} + U_{t,0}, V^{(m)}_{t,0}) = (I_n/2, B, V)$, $L + U = B$ and

$$\begin{pmatrix} 2\widetilde{V}^{(m)}_{t,k} & {}^{\mathrm{t}}\widetilde{L}_{t,k} + {}^{\mathrm{t}}\widetilde{U}_{t,k} + t D_{t,k} \\ \widetilde{L}_{t,k} + \widetilde{U}_{t,k} + t D_{t,k} & 2\widetilde{A}_{t,k} \end{pmatrix} = -t^{-1} J \log(P_{t,k})$$

and

$$P_{t,k} = \left[\prod_{j=1}^{n-1} \begin{pmatrix} I_n + t U^{(j)}_{t,k} & \\ & I_n - t\, {}^{\mathrm{t}}U^{(j)}_{t,k} \end{pmatrix} \right] \begin{pmatrix} I_n & 2t A_{t,k} \\ & I_n \end{pmatrix} \left[\prod_{j=2}^{n} \begin{pmatrix} I_n + t L^{(j)}_{t,k} & \\ & I_n - t\, {}^{\mathrm{t}}L^{(j)}_{t,k} \end{pmatrix} \right] \times \begin{pmatrix} I_n & \\ -2t V^{(m)}_{t,k} & I_n \end{pmatrix}$$

with $L^{(j)}_{t,k} = (e_j \otimes e_j) L_{t,k}$, $U^{(j)}_{t,k} = (e_j \otimes e_j) U_{t,k}$ and $(e_1, \ldots, e_n)$ the canonical basis of $\mathbb{R}^n$.

One can prove that the sequence $(\widetilde{A}_{t,k}, \widetilde{L}_{t,k}, \widetilde{U}_{t,k}, -\frac{t}{2} D_{t,k}, V^{(m)}_{t,k} + \frac{1}{2} D_{t,k})$ generated by this induction converges towards the elements in the exact splitting 1, i.e.

$$|A_t - \widetilde{A}_{t,k}| + |L_t - \widetilde{L}_{t,k}| + |U_t - \widetilde{U}_{t,k}| + |V^{(\ell)}_t + \frac{1}{2} D_{t,k}| + |V^{(r)}_t - V^{(m)}_{t,k} - \frac{1}{2} D_{t,k}| \leq \left(\frac{t}{\tau_0} \right)^k.$$

as soon as t is small enough ($0 < |t| < \tau_0$ for a given $\tau_0 > 0$).

5.3 Extension to More General Schrödinger Equations

Before presenting some numerical results, some time discretizations based on the previous exact splittings are proposed here in order to deal with more general Schrödinger equations. Keeping the same notations $\psi(\mathbf{x}, t) \in \mathbb{C}$ for the unknown ($\mathbf{x} \in \mathbb{R}^n$ and $t \geq 0$), we then consider the following Schrödinger equation to illustrate our strategy

$$i \frac{\partial \psi(\mathbf{x}, t)}{\partial t} = -\frac{1}{2} \Delta \psi(\mathbf{x}, t) - i (B\mathbf{x}) \cdot \nabla \psi(\mathbf{x}, t) + V(\mathbf{x}) \psi(\mathbf{x}, t) + f(\mathbf{x}, |\psi|^2) \psi(\mathbf{x}, t), \quad (23)$$

where f is a real valued function, $B \in A_n(\mathbb{R})$ is a skew symmetric matrix of size n, and $V(\mathbf{x}) : \mathbb{R}^n \to \mathbb{R}$ is a real valued quadratic potential. Some well known examples can be given in the case $n = 2, 3$

- $f(\mathbf{x}, |\psi|^2) = \beta |\psi|^2$ ($\beta \in \mathbb{R}$), $(B\mathbf{x}) \cdot \nabla \psi = \Omega (x_2 \partial_{x_1} - x_1 \partial_{x_2}) \psi$, $\Omega \in \mathbb{R}$. In this case, (23) is the so-called Gross–Pitaevskii equation (GPE) with an angular momentum rotation term (see [9,11]).
- $f(\mathbf{x}, |\psi|^2) = V_{nq}(\mathbf{x})$ where $V_{nq}(\mathbf{x})$ denotes a non-quadratic potential. Moreover, if $V(\mathbf{x}) = \frac{1}{2} |B\mathbf{x}|^2$, (23) is the so-called magnetic Schrödinger equation (see [17,28]).

Algorithm 2 Pseudo-spectral method for ESQM (25)

Input: $\psi^0 = \psi^0_{|\mathbb{G}_1\times\mathbb{G}_2\times\mathbb{G}_3}$, $K\Delta t = T_{final}$
for $k = 0$ to $K-1$ **do**
  $\psi^{(1)} = e^{-i\Delta t/2\ f(g,|\psi^k_g|^2)}\psi^n$
  $\psi^{(2)} = e^{-i\Delta t V^{(r)}_{\Delta t}(g)}\psi^{(1)}$
  $\psi^{(3)} = e^{-i\Delta t\omega_3(L_{\Delta t,31}g_1+L_{\Delta t,32}g_2)}\ \mathcal{F}_3\psi^{(2)}$
  $\psi^{(4)} = e^{-i\Delta t\omega_2 L_{\Delta t,21}g_1}\ \mathcal{F}_2\psi^{(3)}$
  $\psi^{(5)} = e^{-i\Delta t a(\omega)}\ \mathcal{F}_1\psi^{(4)}$
  $\psi^{(6)} = e^{-i\Delta t\omega_2 U_{\Delta t,23}g_3}\ \mathcal{F}_3^{-1}\psi^{(5)}$
  $\psi^{(7)} = e^{-i\Delta t\omega_1(U_{\Delta t,12}g_2+U_{\Delta t,13}g_3)}\ \mathcal{F}_2^{-1}\psi^{(6)}$
  $\psi^{(8)} = e^{-i\Delta t V^{(r)}_{\Delta t}(g)}\ \mathcal{F}_1^{-1}\psi^{(7)}$
  $\psi^{k+1} = e^{-i\Delta t/2\ f(g,|\psi^{(8)}_g|^2)}\psi^{(8)}$
end for
Output: ψ^K
ω_j and g_j are the variables associated with $\mathbb{G}_j$ and $\widehat{\mathbb{G}_j}$ (see end of Sect. 2).

On can show that (23) has the following two conserved quantities,

$$\begin{aligned}&\text{(mass)}\quad M(t) = \int_{\mathbb{R}^n} |\psi(\mathbf{x},t)|^2 d\mathbf{x},\\ &\text{(energy)}\quad E(t) = \int_{\mathbb{R}^n}\Big[\frac{1}{2}|\nabla\psi|^2 + V|\psi|^2 + F(\mathbf{x},|\psi|^2) - \mathrm{Re}(i(B\mathbf{x})\cdot\nabla\psi\ \psi^*)\Big]d\mathbf{x},\end{aligned} \tag{24}$$

where $F(\mathbf{x},\cdot)$ denotes the primitive of $f(\mathbf{x},\cdot)$ vanishing at the origin and f^* and $\mathrm{Re}(f)$ denote the conjugate and real part of the function f respectively.

From the exact splitting presented above, we deduce a new splitting for (23). This splitting is based on Strang composition of the quadratic and the non-quadratic parts. Indeed, we first rewrite (23) as

$$i\partial_t\psi = -p^w\psi + f(\mathbf{x},|\psi|^2)\psi,$$

where $-p^w\psi := -\frac{1}{2}\Delta\psi - i(B\mathbf{x})\cdot\nabla\psi + V(\mathbf{x})\psi$ denotes the quadratic part (in the sense of Sect. 2) and $f(\mathbf{x},|\psi|^2)\psi$ denotes the non quadratic part (which can be nonlinear). Based on this formulation and on the fact that exact splittings have been derived for the quadratic part, we then propose the following splitting (ESQM method) for $k \geq 0$

$$(\psi(\mathbf{x},t_k) \approx)\psi^k(\mathbf{x}) = \Big(e^{-i\frac{\Delta t}{2}f(\mathbf{x},|\cdot|^2)}e^{-i\Delta t p^w}e^{-i\frac{\Delta t}{2}f(\mathbf{x},|\cdot|^2)}\Big)^k\psi_0(\mathbf{x}), \tag{25}$$

where the computation of $e^{-i\Delta t p^w}$ is done using (21) and $e^{-i\frac{\Delta t}{2}f(\mathbf{x},|\cdot|^2)}$ denotes the nonlinear operator defined by $e^{-i\frac{\Delta t}{2}f(\mathbf{x},|\cdot|^2)}\psi = e^{-i\frac{\Delta t}{2}f(\mathbf{x},|\psi|^2)}\psi$. Let us remark that for this Strang based splitting, each part can be solved exactly in time and arbitrary high order time integrators can be constructed by composition methods (see [21]). It can also be shown that the L^2 norm of ψ^k is preserved by the numerical schemes proposed here. In Algorithm 2, we detail the different substeps of the splitting (25) involving the pseudo-spectral discretization in dimension 3.

Remark 4 Note that some optimizations can be performed in Algorithm 2 by noticing the following rearrangement (with $K\Delta t = T_{\text{final}}$)

$$\begin{aligned}\psi^K &= \left(e^{-i\frac{\Delta t}{2}f(\mathbf{x},|\cdot|^2)}e^{i\Delta t(-V(\mathbf{x})+\frac{\Delta}{2}-B\mathbf{x}\cdot\nabla)}e^{-i\frac{\Delta t}{2}f(\mathbf{x},|\cdot|^2)}\right)^K\psi^0\\ &= e^{-i\frac{\Delta t}{2}f(\mathbf{x},|\cdot|^2)-i\Delta tV_{\Delta t}^{(\ell)}(\mathbf{x})}e^{-t(U_{\Delta t}\mathbf{x})_1\partial_{x_1}}e^{-t(U_{\Delta t}\mathbf{x})_2\partial_{x_2}}e^{itA_{\Delta t}(\nabla)}e^{-\Delta t(L_{\Delta t}\mathbf{x})_2\partial_{x_2}}e^{-\Delta t(L_t\mathbf{x})_3\partial_{x_3}}\\ &\left(e^{-i\Delta tf(\mathbf{x},|\cdot|^2)-i\Delta tV_{\Delta t}^{(\ell)}(\mathbf{x})-i\Delta tV_{\Delta t}^{(r)}(\mathbf{x})}e^{-\Delta t(U_{\Delta t}\mathbf{x})_1\partial_{x_1}}e^{-\Delta t(U_{\Delta t}\mathbf{x})_2\partial_{x_2}}e^{i\Delta tA_{\Delta t}(\nabla)}\right.\\ &\left.e^{-\Delta t(L_{\Delta t}\mathbf{x})_2\partial_{x_2}}e^{-\Delta t(L_{\Delta t}\mathbf{x})_3\partial_{x_3}}\right)^{K-1}e^{-i\Delta tV_{\Delta t}^{(r)}(\mathbf{x})-i\frac{\Delta t}{2}f(\mathbf{x},|\psi^0|^2)}\psi^0.\end{aligned} \tag{26}$$

5.4 Numerical Results

This section is devoted to applications of exact splittings to the Schrödinger type equations (23) both in the two and three dimensional cases. We show higher accuracy and efficiency of the exact splittings by comparing with other usual numerical methods proposed in the literature [10,11].

As previously, the space discretization requires a truncated domain denoted by $[-R_1, R_1]\times\cdots\times[-R_n, R_n]$. We will consider a uniform grid with N_j points per direction so that the mesh size are $2R_j/N_j$.

5.4.1 2D Schrödinger Equations

Firstly, we consider the application of the exact splittings in the two-dimensional case on the magnetic Schrödinger equation and on the rotating Gross–Pitaevskii equation.

2D magnetic Schrödinger equation

In this numerical experiment, following 2D magnetic Schrödinger equation is considered [28],

$$i\epsilon\partial_t\psi(\mathbf{x},t) = -\frac{\epsilon^2}{2}\Delta\psi(\mathbf{x},t) + i\epsilon\mathbf{A}\cdot\nabla\psi(\mathbf{x},t) + \frac{1}{2}|\mathbf{A}|^2\psi(\mathbf{x},t), \tag{27}$$

with $\epsilon = 1/32$, $\mathbf{x} = (x_1, x_2) \in \mathbb{R}^2$, and $\mathbf{A} = \frac{1}{2}{}^t(-x_2, x_1)$. The initial condition is given by

$$\psi_0(\mathbf{x}) = e^{-20(x_1-0.05)^2-20(x_2-0.1)^2}e^{i\sin(x_1)\sin(x_2)/\epsilon}.$$

The numerical parameters are chosen as follows: $N_1 = N_2 = 256$, $R_1 = R_2 = 3\pi$ and $\Delta t = 0.3$. We shall compare three different splittings:

- ESQM (see (25) with $f = 0$ and (21)); this method is exact in time.
- ESR (see "Appendix 2"); this method is second order accurate in time.
- Strang (see "Appendix 2"); this method is second order accurate in time.

Let us remark that ESR and Strang are two operator splittings which differ from the treatment of the rotation part $\partial_t\psi = \mathbf{A}\cdot\nabla\psi$. Indeed, this part is solved exactly in the ESR method (this is the reason why we used the same name as in Sect. 3) whereas a second order directional splitting is used in the Strang method. We refer to "Appendix 2" for details. From (21), the ESQM is

$$e^{i\epsilon\Delta t(\frac{\Delta}{2}-\frac{1}{2\epsilon^2}|\mathbf{A}|^2)+\Delta t\mathbf{A}\cdot\nabla} = e^{-\epsilon\Delta tv^{(\ell)}(\mathbf{x})}e^{-\epsilon\Delta t(U_{\Delta t}\mathbf{x})_1\partial x_1}e^{i\epsilon\Delta ta(\nabla)}e^{-\epsilon\Delta t(L_{\Delta t}\mathbf{x})_2\partial_{x_2}}e^{-\epsilon\Delta tv^{(r)}(\mathbf{x})},$$

where $v^{(\ell)}(\mathbf{x}) = {}^t\mathbf{x}V_{\Delta t}^{(\ell)}\mathbf{x}$, $v^{(r)}(\mathbf{x}) = {}^t\mathbf{x}V_{\Delta t}^{(r)}\mathbf{x}$, and $a(\nabla) = \nabla\cdot(A_{\Delta t}\nabla)$, $V_{\Delta t}^{(\ell)}$, $L_{\Delta t}$, $U_{\Delta t}$, $V_{\Delta t}^{(r)}$, $A_{\Delta t}$ are the following 2×2 matrices ($\Delta t = 0.3$)

$$
\begin{aligned}
A_{\Delta t} &\simeq \begin{pmatrix} 0.503532819405421 & -0.074439184790650 \\ -0.074439184790650 & 0.503784060194312 \end{pmatrix},\\
L_{\Delta t} &\simeq \begin{pmatrix} 0 & 0 \\ -16.121089926218119 & 0 \end{pmatrix}, \quad U_{\Delta t} \simeq \begin{pmatrix} 0 & 15.761077688604765 \\ 0 & 0 \end{pmatrix},\\
V_{\Delta t}^{(\ell)} &\simeq \begin{pmatrix} 128.9687194097432 & 0 \\ 0 & -0.0000000000018 \end{pmatrix},\\
V_{\Delta t}^{(r)} &\simeq \begin{pmatrix} 2.8800979009085 & -19.0564313064080 \\ -19.0564313064080 & 126.0886215088400 \end{pmatrix}.
\end{aligned}
$$

First of all, we show the contour plots of $|\psi(\mathbf{x},t)|^2$ at time $t = 300$ in Fig. 6 obtained by these three methods. Second, the time history of energy error (defined by (24)) given by these three methods is presented in Fig. 7. As (27) is a quadratic equation, by Theorem 1, the ESQM method gives the exact solution (if neglecting space error). From Fig. 7, we can see that its energy error is at machine precision level, which is much smaller than the energy errors of Strang and ESR. Specifically, as the rotation velocity of Strang is not correct (see [13]), we can see in Fig. 6 that the contour plot obtained by Strang is not good. For ESR, even if the rotation velocity is right and the shape of the solution has the correct orientation, error is clearly observed.

2D rotating Gross–Pitaevskii equation

We now consider the dynamics of rotating Bose–Einstein condensates, which is described by the following rotating Gross–Pitaevskii equation (GPE) (see [9,11])

$$
i\partial_t\psi(\mathbf{x},t) = -\frac{1}{2}\Delta\psi(\mathbf{x},t) + V(\mathbf{x})\psi(\mathbf{x},t) + \beta|\psi|^2\psi(\mathbf{x},t) - \Omega L_{x_3}\psi(\mathbf{x},t), \quad \psi(\mathbf{x},0) = \psi_0(\mathbf{x}) \tag{28}
$$

where $\psi(\mathbf{x},t)$ ($\mathbf{x} = (x_1,x_2) \in \mathbb{R}^2, t \geq 0$) is wave function , $L_{x_3} = -i(x_1\partial_{x_2} - x_2\partial_{x_1})$ is the x_3-component of the angular momentum, Ω is the angular speed of the laser beam, β is a constant characterizing the particle interactions, and $V(\mathbf{x})$ denotes the external harmonic oscillator potential

$$
V(\mathbf{x}) = \frac{1}{2}(\gamma_{x_1}^2x_1^2 + \gamma_{x_2}^2x_2^2), \quad \gamma_{x_1} > 0,\ \gamma_{x_2} > 0. \tag{29}
$$

In addition to the mass and energy conservations (24), the expectation of angular momentum is also conserved when $\gamma_{x_1} = \gamma_{x_2}$

$$
Lz(t) := \int_{\mathbb{R}^2} \psi^*(\mathbf{x},t)L_{x_3}\psi(\mathbf{x},t)d\mathbf{x} = Lz(0). \tag{30}
$$

We are also interested in the time evolution of condensate widths and mass center defined as follows,

$$
\begin{aligned}
&\text{condensate widths}: \ S_\alpha(t) = \sqrt{\int_{\mathbb{R}^2} \alpha^2|\psi(\mathbf{x},t)|^2d\mathbf{x}}, \quad \alpha = x_1, x_2,\\
&\text{mass center}: \mathbf{x}_c(t) = \int_{\mathbb{R}^2} \mathbf{x}|\psi(\mathbf{x},t)|^2d\mathbf{x}.
\end{aligned} \tag{31}
$$

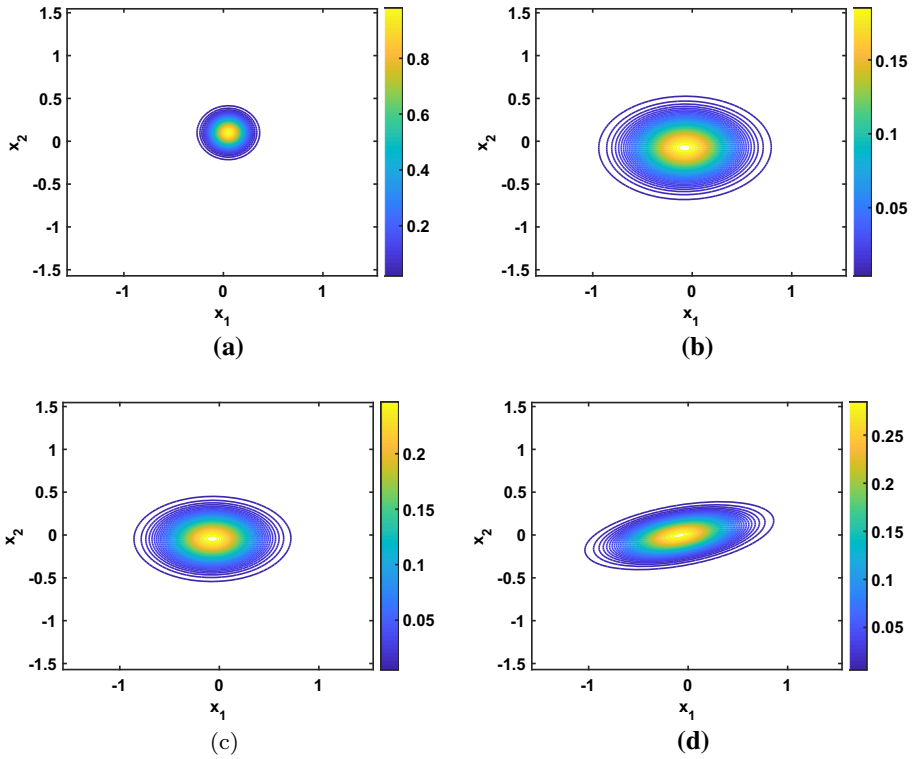

Fig. 6 Contour plots of density $|\psi(\mathbf{x})|^2$ **a** at $t = 0$; computed by **b** ESQM; **c** ESR and **d** Strang method at $t = 300$ with $\Delta t = 0.3$, $N_1 = N_2 = 256$, $\epsilon = \frac{1}{32}$ for 2D magnetic Schrödinger problem

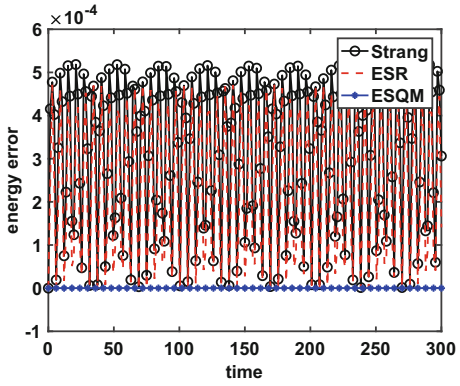

Fig. 7 Time evolution of energy error of ESR, ESQM and Strang splitting method with $\Delta t = 0.3$, $N_1 = N_2 = 256$ and $\epsilon = \frac{1}{32}$ for 2D magnetic Schrödinger equation

For the two dimensional rotating GPE (28), our first numerical test is the so-called dynamics of a stationary state with a shifted center [9]. We take $\gamma_{x_1} = \gamma_{x_2} = 1$, $\beta = 100$ in (28) and the initial condition is taken as

$$\psi_0(\mathbf{x}) = \phi_e(\mathbf{x} - \mathbf{x}_0),$$

where $\phi_e(\mathbf{x})$ is a ground state computed numerically by using the method proposed in [35] and $\mathbf{x}_0 = {}^t(1, 1)$. The numerical parameters are chosen as follows: $\Delta t = 0.001$ and the spatial domain $[-8, 8]^2$ is discretized using $N_1 = N_2 = 256$ points.

There are many accurate and efficient numerical methods in the literature for the rotating Gross–Pitaevskii equation, such as [6–11,14,15]. Similar to the magnetic Schrödinger case, we will consider different methods to solve (28) and compare with our approach

- ESQM (see (25) with $f(\mathbf{x}, |\psi|^2) = \beta|\psi|^2$ and (21)); this method is second order accurate in time.
- Lagrangian from [10] (see "Appendix 2"); this method is second order accurate in time.
- BW from [11] (see "Appendix 1"); this method is second order accurate in time.

Concerning ESQM, we show how the quadratic part $p^w := (i/2)\Delta - \Omega L_{x_3} - iV(\mathbf{x})$ of the nonlinear equation (28) is split. This is done as follows (two cases $\Omega = -0.5$ and $\Omega = 0$ are considered)

$$e^{i\Delta t p^w} = e^{-\Delta t v^{(\ell)}(\mathbf{x})} e^{-\Delta t (U_{\Delta t}\mathbf{x})_1 \partial_{x_1}} e^{i\Delta t a(\nabla)} e^{-\Delta t (L_{\Delta t}\mathbf{x})_2 \partial_{x_2}} e^{-\Delta t v^{(r)}(\mathbf{x})},$$

where $v^{(\ell)}(\mathbf{x}) = {}^t\mathbf{x}V_{\Delta t}^{(\ell)}\mathbf{x}$, $v^{(r)}(\mathbf{x}) = {}^t\mathbf{x}V_{\Delta t}^{(r)}\mathbf{x}$, and $a(\nabla) = \nabla\cdot(A_{\Delta t}\nabla)$, $V_{\Delta t}^{(\ell)}$, $L_{\Delta t}$, $U_{\Delta t}$, $V_{\Delta t}^{(r)}$, $A_{\Delta t}$ being 2×2 matrices. In the case $\Omega = -0.5$, we have

$$A_{\Delta t} \simeq \begin{pmatrix} 0.499999979166548 & 0.000249999947774 \\ 0.000249999947774 & 0.499999979166793 \end{pmatrix},$$

$$L_{\Delta t} \simeq \begin{pmatrix} 0 & 0 \\ 0.500000041666437 & 0 \end{pmatrix}, \quad U_{\Delta t} \simeq \begin{pmatrix} 0 & -0.499999916666871 \\ 0 & 0 \end{pmatrix},$$

$$V_{\Delta t}^{(\ell)} \simeq \begin{pmatrix} 0.312500037655718 & 0 \\ 0 & 0.187500011768640 \end{pmatrix},$$

$$V_{\Delta t}^{(r)} \simeq \begin{pmatrix} 0.187500043073584 & 0.000062500002635 \\ 0.000062500002635 & 0.312500006460442 \end{pmatrix},$$

and in the case $\Omega = 0$, we have

$$A_{\Delta t} \simeq \begin{pmatrix} 0.499999916666670 & 0 \\ 0 & 0.499999916666676 \end{pmatrix},$$

$$L_{\Delta t} = \begin{pmatrix} 0 & 0 \\ 0 & 0 \end{pmatrix}, \quad U_{\Delta t} = \begin{pmatrix} 0 & 0 \\ 0 & 0 \end{pmatrix},$$

$$V_{\Delta t}^{(\ell)} \simeq \begin{pmatrix} 0.250000020830159 & 0 \\ 0 & 0.250000020843983 \end{pmatrix},$$

$$V_{\Delta t}^{(r)} \simeq \begin{pmatrix} 0.250000020836518 & 0 \\ 0 & 0.250000020822696 \end{pmatrix}.$$

We first validate our ESQM approach by plotting the time evolutions of mass center, condensate widths (31), and angular momentum expectation error (30) in Fig. 8. We can see that time evolution of mass center is periodic, and the period is equal to 2π (resp. 4π) when $\Omega = 0$ (resp. $\Omega = -0.5$), which is in good agreement to the results in [9].

In the sequel, we compare ESQM with Lagrangian and BW. Both ESQM and Lagrangian method need 4 FFT for each time step whereas BW needs 6. As the FFT calls are the most consuming part of the three methods, ESQM and Lagrangian are the most efficient methods. The energy error (24) and angular momentum expectation error (30) with different time step sizes of the three methods (Lagrangian, ESQM and BW) are presented in Fig. 9 for $\Omega = -0.5$ and with different values of the nonlinearity factor ($\beta = 5$ and $\beta = 100$). First, we notice that

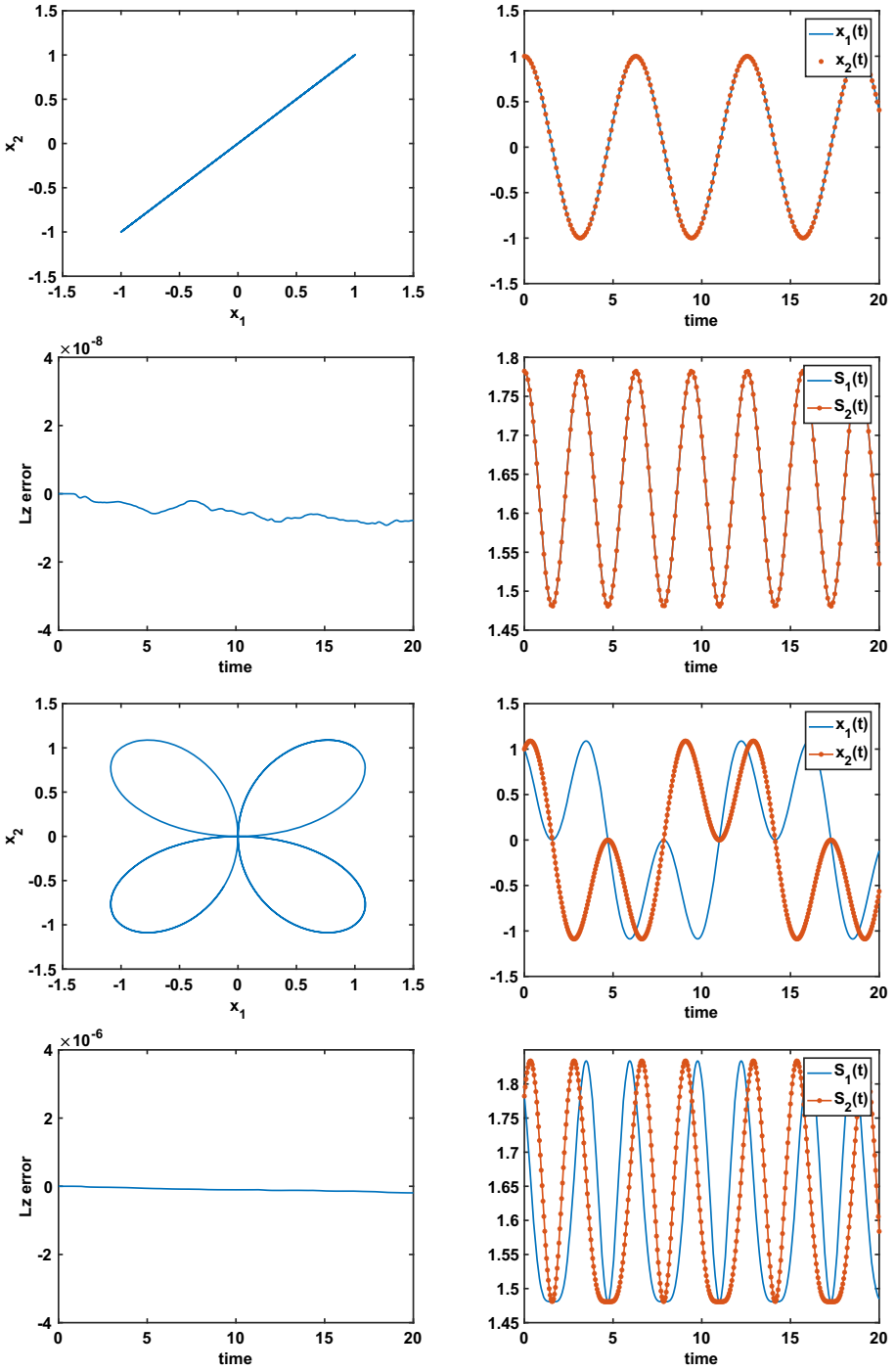

Fig. 8 Time evolution of mass center, coordinates of mass center, error on angular momentum expectation, and condensate widths by ESQM when $\Omega = 0$ (top four figures) and $\Omega = -0.5$ (bottom four figures)

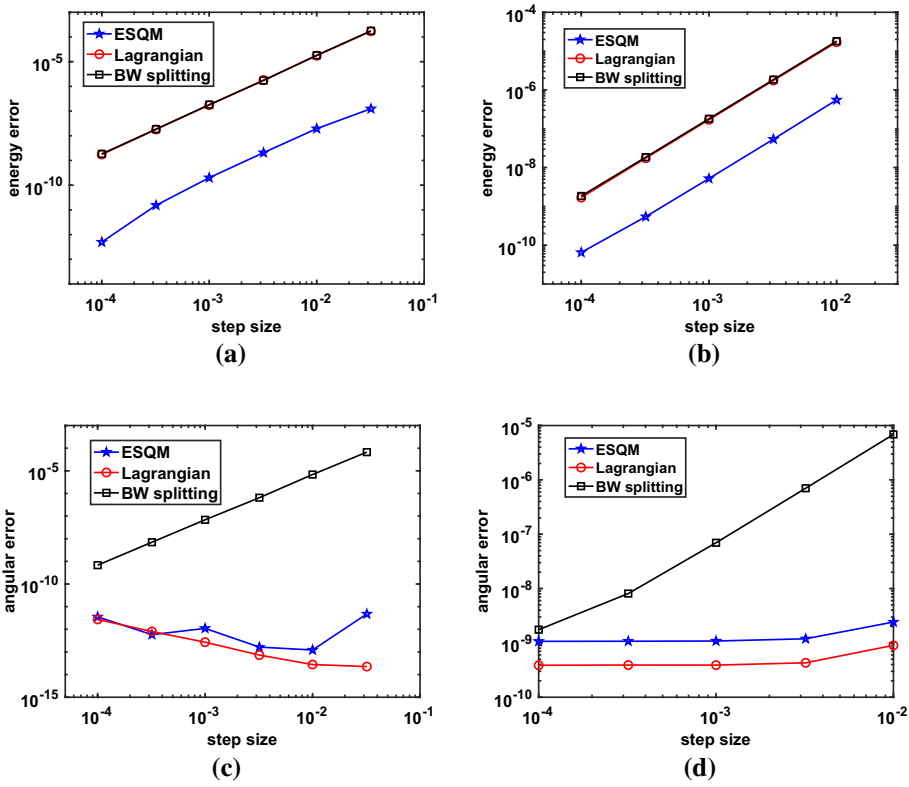

Fig. 9 Energy error and angular momentum expectation error (semi-$\log_{10}$ scale) as a function of the step size for the three methods ESQM, Lagrangian and BW at $t = 1$ for $\Omega = -0.5$, when $\beta = 5$, (a,c), $\beta = 100$, (b,d)

these three methods are second order accurate regarding the energy as expected. However, the error of ESQM is much smaller (two orders of magnitude smaller), which is due to the fact that the linear part is solved exactly. Moreover, the advantage of ESQM is more obvious when the nonlinearity factor β is smaller. For the angular moment expectation conservation, we can see that BW is still second order in time, whereas the error of Lagrangian and ESQM is close to the machine precision. The reason is that angular moment expectation is conserved by the solution of each subsystem in ESQM and Lagrangian (see [9] for more details).

To end this part, we focus on the second numerical experiment, in which the time evolution of a ground state is studied by changing the corresponding potential initially as [3,15]. The parameters are $\beta = 1000$, $\Omega = 0.9$, the potential is given by (29) with $\gamma_{x_1} = 1.05$, $\gamma_{x_2} = 0.95$. The initial condition is the ground state corresponding to the isotropic potential $V(\mathbf{x}) = |\mathbf{x}|^2/2$, $\beta = 1000$, and $\Omega = 0.9$, generated using the Matlab toolbox GPELab[1]. [4,5]. In this numerical test, we only use ESQM and consider the numerical parameters as follows: the spatial grid is defined by $[-8, 8]^2$, $N_1 = N_2 = 128$, and the time step size is $\Delta t = 10^{-3}$. The coefficients for ESQM in (21) are given by

$$A_{\Delta t} \simeq \begin{pmatrix} 0.500000110624718 & -0.000449999864087 \\ -0.000449999864087 & 0.500000127291716 \end{pmatrix},$$

[1] http://gpelab.math.cnrs.fr

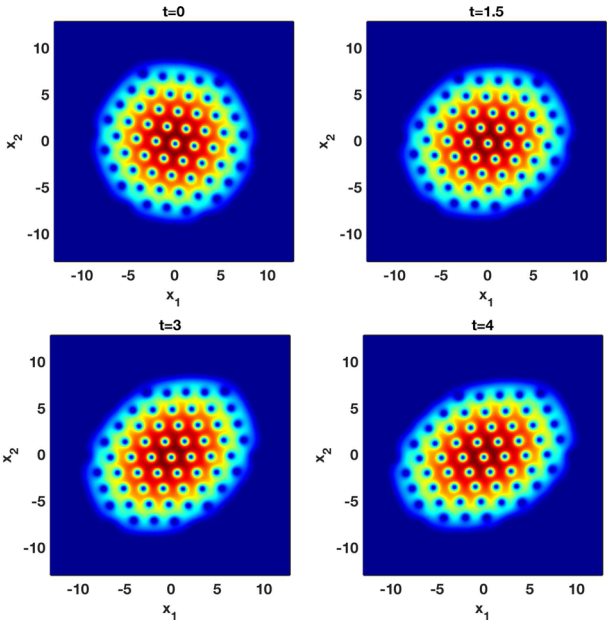

Fig. 10 $\beta = 1000, \Omega = 0.9$. Time evolution of the solution of (28) by changing the potential initially

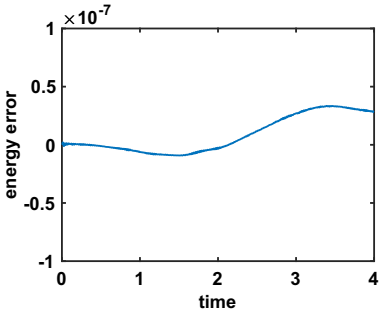

Fig. 11 $\beta = 1000, \Omega = 0.9$. Time evolution of the energy of (28) by changing the potential initially

$$L_{\Delta t} \simeq \begin{pmatrix} 0 & 0 \\ -0.900000273000100 & 0 \end{pmatrix}, \quad U_{\Delta t} \simeq \begin{pmatrix} 0 & 0.899999484000032 \\ 0 & 0 \end{pmatrix},$$
$$V_{\Delta t}^{(\ell)} \simeq \begin{pmatrix} 0.478125137872035 & 0 \\ 0 & 0.023124993175043 \end{pmatrix},$$
$$V_{\Delta t}^{(r)} \simeq \begin{pmatrix} 0.073125336336629 & -0.000364499913716 \\ -0.000364499913716 & 0.428124781225271 \end{pmatrix}.$$

The contour plots of $|\psi(\mathbf{x}, t)|^2$ are plotted for different times ($t = 0, 1.5, 3, 4$) in Fig. 10. These results are in very good agreement with those obtained in the literature [3,15]. We also present in Fig. 11 the time evolution of the energy error, from which we can see that energy conservation is very good (about 10^{-7}).

5.4.2 3D Schrödinger Equations

In this section, 3D Schrödinger equations are considered in two cases: (i) a quadratic Schrödinger equation is constructed specifically such that the solution is periodic in time; (ii) a magnetic Schrödinger equation with a non-quadratic potential (see [17]).

3D time-periodic quadratic linear Schrödinger equation

For (23), we consider $f = 0$ and

$$B = \frac{\pi}{3}\begin{pmatrix} 0 & -1 & 1 \\ 1 & 0 & -1 \\ -1 & 1 & 0 \end{pmatrix} \quad \text{and} \quad V(\mathbf{x}) = \frac{\pi^2}{9}\,{}^t\mathbf{x}\begin{pmatrix} \lambda_1 & & \\ & \lambda_2 & \\ & & \lambda_3 \end{pmatrix}\mathbf{x}, \tag{32}$$

where $\mathbf{x} = (x_1, x_2, x_3)$ and $(\lambda_1, \lambda_2, \lambda_3)$ are the roots of the polynomial $Q(X) = 7200X^3 - 72196X^2 + 222088X - 216341$, i.e.

$$\begin{pmatrix} \lambda_1 \\ \lambda_2 \\ \lambda_3 \end{pmatrix} \simeq \begin{pmatrix} 2.27017996551810 \\ 2.53418020791380 \\ 5.22286204879033 \end{pmatrix}. \tag{33}$$

In this case, the period of this system is $T = 360$ (see in "Appendix 6" for the proof) and the initial condition is

$$\psi_0(x_1, x_2, x_3) = \left(\frac{2}{\pi}\right)^3 e^{-x_1^2} e^{-2x_2^2} e^{-2(x_3-1)^2} + i\left(\frac{2}{\pi}\right)^3 e^{-x_1^2} e^{-2(x_2+1)^2} e^{-2(x_3-1)^2}. \tag{34}$$

The numerical parameters are chosen as: spatial domain $[-8, 8]^3$ is discretized by $N_1 = N_2 = N_3 = 96$ points, time step is $\Delta t = 0.2$, and final time is $t = 720$ which corresponds to two periods $2T$. We consider following two numerical methods:

- ESQM from (21) whose coefficients are listed in "Appendix 1"; the method is exact in time.
- Strang (see in "Appendix 2"); the method is second order accurate in time.

In Figs. 12 and 13, the time evolutions of $|\psi(t, 0, 0, 0)|^2$ are presented by using ESQM and Strang respectively. We also plot the difference $|\psi(t \in [T, 2T], 0, 0, 0)|^2 - |\psi(t \in [0, T], 0, 0, 0)|^2$ which should be zero since the solution is time periodic of period $T = 360$. We can see that for ESQM, the period is nicely preserved (up to 10^{-11}) in spite of the fact that the time history of the solution is quite complicated. However, one can observe in Fig. 13 that the error of Strang method is too large to identify the period. In Fig. 14, the time history of energy error is plotted for both ESQM and Strang methods. Clearly, Strang method produces larger error. Some contour plots of the solution (at time $t = 360$ and the third spatial direction x_3 is fixed to be 0) obtained by ESQM and Strang are presented at Fig. 15. Note that $\psi(t = 360, x_1, x_2, 0)$ is the same as the initial condition since the solution is 360 periodic in time. In Fig. 15, we can see that ESQM gives very accurate results, but the result obtained by Strang method is rather different. Concerning the computational cost, 6 FFT (or inverse) are required for each time step for ESQM whereas Strang needs 15 FFT (or inverse).

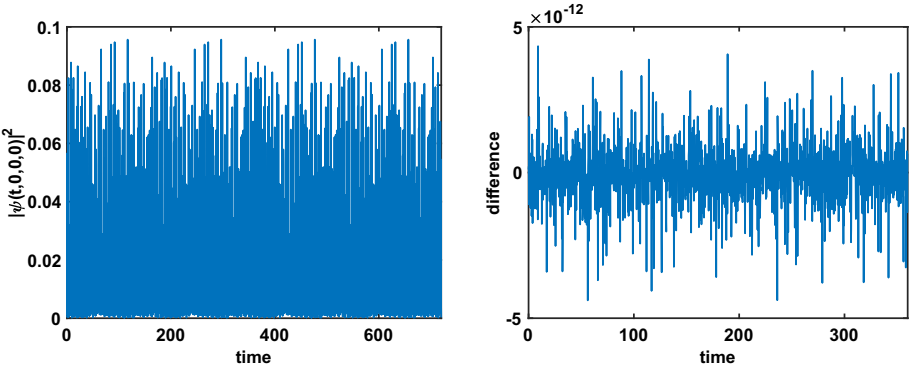

Fig. 12 ESQM: **a** Time evolution of $|\psi(t,0,0,0)|^2$. **b** The difference $|\psi([T,2T],0,0,0)|^2 - |\psi([0,T],0,0,0)|^2$, $T = 360$

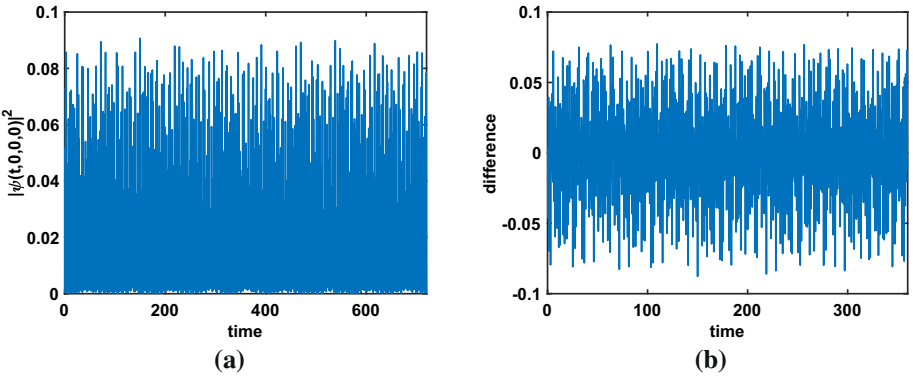

Fig. 13 Strang: **a** Time evolution of $|\psi(t,0,0,0)|^2$. **b** The difference $|\psi([T,2T],0,0,0)|^2 - |\psi([0,T],0,0,0)|^2$, $T = 360$

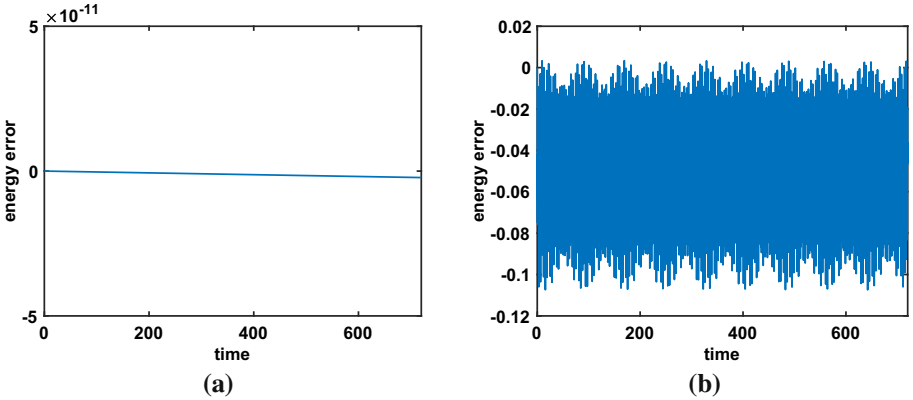

Fig. 14 **a** Time evolution of the energy error by ESQM. **b** Time evolution of the energy error by Strang splitting

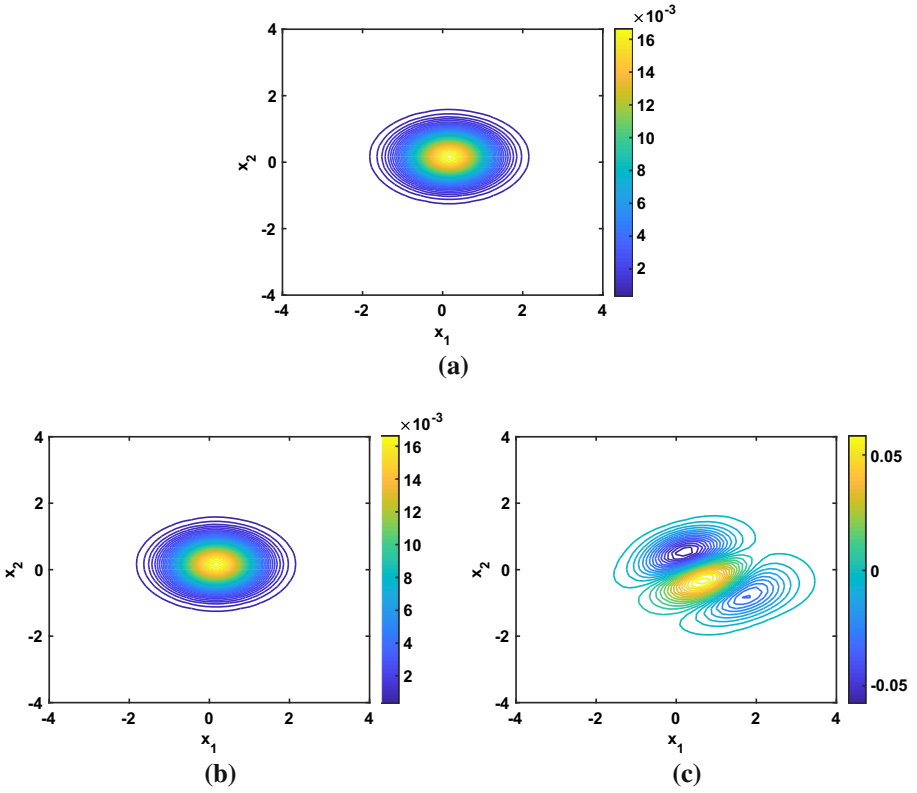

Fig. 15 **a** Initial contour plot of the real part of $\psi(t = 0, x_1, x_2, 0)$; **b** contour plot of real part of $\psi(t = 360, x_1, x_2, 0)$ by ESQM; **c** contour plot of real part of $\psi(t = 360, x_1, x_2, 0)$ by Strang

3D magnetic Schrödinger equation

To end this part, the following 3D magnetic Schrödinger equation is considered (see [17]),

$$i\,\partial_t \psi(\mathbf{x}, t) = -\frac{1}{2}\Delta\psi(\mathbf{x}, t) + i\,\mathbf{A}(\mathbf{x}) \cdot \nabla\psi(\mathbf{x}, t) + \frac{1}{2}|\mathbf{A}(\mathbf{x})|^2\psi(\mathbf{x}, t) + V_{nq}(\mathbf{x})\psi(\mathbf{x}, t), \tag{35}$$

where $\mathbf{A}(\mathbf{x}) = \mathbf{x} \times \mathbf{B}$, $\mathbf{B} = {}^t(1, 0.1, 2)$, $\mathbf{x} = (x_1, x_2, x_3)$ and

$$V_{nq}(\mathbf{x}) = \alpha\left(20\cos(\frac{2\pi(x_1+5)}{10}) + 20\cos(\frac{2\pi(x_2+5)}{10}) + 20\cos(\frac{2\pi(x_3+5)}{10}) + 60\right), \alpha \in \mathbb{R}. \tag{36}$$

The initial condition is

$$\psi_0(\mathbf{x}) = \frac{2^{3/8}}{\pi^{3/2}}\exp\left(-\frac{\sqrt{2}}{2}((x_1-1)^2 + x_2^2 + x_3^2)\right),$$

and the numerical parameters are: the spatial domain $[-5, 5]^3$, $N_1 = N_2 = N_3 = 64$, and the final time $t = 1$. Here we consider three methods

– ESQM (see (25) with $f(\mathbf{x}, |\psi|^2) = V_{nq}(\mathbf{x})$ given by (36) and with (21)); this method is second order accurate in time.

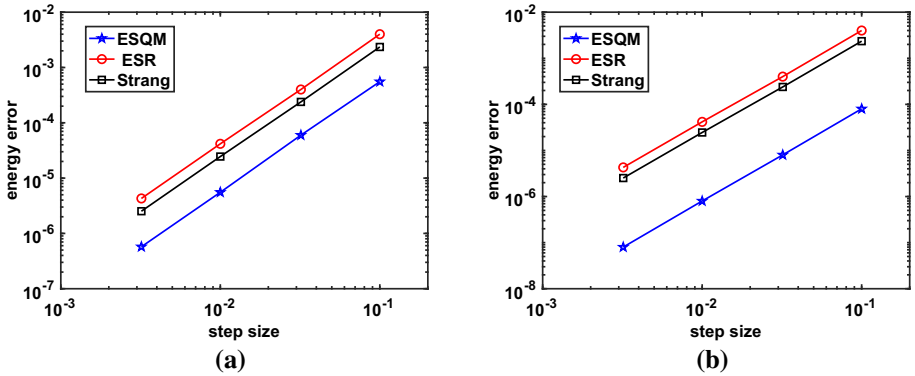

Fig. 16 Plots of energy error with step size at $t = 1$ with grids $N_1 = N_2 = N_3 = 64$. (a) $\alpha = 0.1$, (b) $\alpha = 0.01$

– ESR (see "Appendix 5"); this method is second order accurate in time.
– Strang (see "Appendix 5"); this method is second order accurate in time.

The three methods are compared with different step sizes Δt to solve the system (35). The time evolutions of energy error of these three methods are presented in Fig. 16, with different parameter α which measures the amplitude of the non-quadratic part in (35). By comparing the energy error, we can see that the ESQM is the most accurate one, as it solves the linear quadratic part exactly. Moreover, when α is smaller, i.e., the non-quadratic term in system (35) becomes smaller, the advantage of ESQM is more obvious.

Compliance with Ethical Standards

Conflict of interest The authors declare that they have no conflict of interest.

Appendix

Backward Error Analysis of the Strang Splittings for Rotations

We consider the ODE associated with a rotation in $\mathbb{R}^n$

$$\dot{y} = By \tag{37}$$

where $B \in \mathfrak{so}_n(\mathbb{R})$ is a real skew-symmetric matrix of size n. For $t \in \mathbb{R}$, the Strang splitting naturally associated with the decomposition of this rotation in shear transforms is

$$P_t = \left(\prod_{j=1}^{n-1} \mathrm{I}_n + \frac{t}{2}(e_j \otimes e_j)B\right)(\mathrm{I}_n + t(e_n \otimes e_n)B)\left(\prod_{j=1}^{n-1} \mathrm{I}_n + \frac{t}{2}(e_{n-j} \otimes e_{n-j})B\right).$$

where $e_1, \ldots, e_n$ is the canonical basis of $\mathbb{R}^n$. It is indeed a Strang splitting because since $(e_j \otimes e_j)B$ is nilpotent of order 1 we have

$$e^{t(e_j \otimes e_j)B} = \mathrm{I}_n + t(e_j \otimes e_j)B.$$

The following proposition states that, up to a change of coordinate close to the identity, P_t is a rotation of which angles coincide with those of $\exp(tB)$ up to an error of order t^3.

Proposition 2 *There exists $t_0 > 0$ and two analytic functions $t \in (-t_0, t_0) \mapsto (B_t, Q_t) \in \mathfrak{so}_n(\mathbb{R}) \times \mathrm{S}_n(\mathbb{R}) \cap \mathrm{GL}_n(\mathbb{R})$, where B_t is real skew symmetric and Q_t is real symmetric and invertible such that $B_0 = B$, $Q_0 = \mathrm{I}_n$ and*

$$\forall t \in (-t_0, t_0),\ P_t = Q_{t^2} e^{t B_{t^2}} Q_{t^2}^{-1}.$$

Proof Observing that since

$$\mathfrak{sp}(B) = \{SB \mid S \in \mathrm{S}_n(\mathbb{R})\} \text{ is a Lie algebra,}$$

it follows from the Bakker-Campbell-Hausdorff formula that there exist $t_1 > 0$ and an analytic function $t \in (-t_1, t_1) \mapsto S_t \in \mathrm{S}_n(\mathbb{R})$ such that $S_0 = \mathrm{I}_n$ and

$$\forall t \in (-t_1, t_1),\ P_t = e^{t S_t B}.$$

Since the Strang splitting is reversible, we have $P_t = P_{-t}^{-1}$. Thus, since the exponential map is injective in a neighborhood of the identity, we deduce that $t \mapsto S_t$ is an even function. Consequently, there exists an analytic function $t \mapsto K_t$ such that $K_{t^2} = S_t$. Furthermore, since $K_0 = \mathrm{I}_n$, there exists $t_0 \in (0, t_1)$ such that for all $t \in (-t_0, t_0)$, K_t is positive-definite. Finally, we deduce that,

$$\forall t \in (-t_0, t_0),\ P_t = e^{t S_t B} = \sqrt{K_{t^2}} e^{t \sqrt{K_{t^2}} B \sqrt{K_{t^2}}} \sqrt{K_{t^2}}^{-1} = Q_{t^2} e^{t B_{t^2}} Q_{t^2}^{-1}$$

where $Q_t = \sqrt{K_t}$ and $B_t = \sqrt{K_t} B \sqrt{K_t}$. □

2D Magnetic Schrödinger Equation

$$i\epsilon \partial_t \psi(\mathbf{x}, t) = -\frac{\epsilon^2}{2} \Delta \psi(\mathbf{x}, t) + i\epsilon \mathbf{A} \cdot \nabla \psi(\mathbf{x}, t) + \frac{1}{2} |\mathbf{A}|^2 \psi(\mathbf{x}, t), \tag{38}$$

where $\mathbf{x} = (x_1, x_2) \in \mathbb{R}^2$, $\mathbf{A} = \frac{1}{2}(A_1, A_2)$, $A_1 = -x_2$, $A_2 = x_1$. The above system can be split into three systems:

$$i\epsilon \partial_t \psi(\mathbf{x}, t) = -\frac{\epsilon^2}{2} \Delta \psi(\mathbf{x}, t), \tag{39}$$

$$\partial_t \psi(\mathbf{x}, t) = \mathbf{A} \cdot \nabla \psi(\mathbf{x}, t), \tag{40}$$

$$i\epsilon \partial_t \psi(\mathbf{x}, t) = \frac{1}{2} |\mathbf{A}|^2 \psi(\mathbf{x}, t), \tag{41}$$

The solutions of the above three subsystems can be obtained by operators $e^{it\frac{\epsilon}{2}\Delta}$, $e^{t\mathrm{Rot}}$, and e^{tV} respectively. Since the second is nothing but a 2D rotation, we call the associated solution $e^{t\mathrm{Rot}}$. Then we have the following second order splitting method

$$\psi^{n+1} = e^{\frac{\Delta t}{2} V} e^{i \Delta t \frac{\epsilon}{4} \Delta} e^{\Delta t \mathrm{Rot}} e^{i \Delta t \frac{\epsilon}{4} \Delta} e^{\frac{\Delta t}{2} V}, \tag{42}$$

from which we derive two variants according to the treatment of $e^{\Delta t \mathrm{Rot}}$. Indeed, **ESR** denotes the splitting method (42) when $e^{\Delta t \mathrm{Rot}}$ is solved by exact splittings for transport equation in Proposition 1. **Strang** denotes (42) when $e^{\Delta t \mathrm{Rot}}$ is approximated by Strang directional splitting.

2D Rotating Gross–Pitaevskii Equation

The rotating Gross-Pitaevskii equation (GPE) [9,11] is

$$i\partial_t \psi(\mathbf{x},t) = -\frac{1}{2}\Delta\psi(\mathbf{x},t) + V(\mathbf{x})\psi(\mathbf{x},t) + \beta|\psi|^2\psi(\mathbf{x},t) - \Omega L_{x_3}\psi(\mathbf{x},t),\ \mathbf{x}\in\mathbb{R}^2, \quad (43)$$

where $\psi(\mathbf{x},t)$ is the macroscopic wave function, $\mathbf{x} = (x_1, x_2)$, $L_{x_3} = -i(x_1\partial_{x_2} - x_2\partial_{x_1})$. Two operator splittings are presented to approximate (43).

BW Method

Here we recall the splitting method introduced in [11] to approximate (43). We will call it BW in the sequel. BW splitting for rotating GPE (43) is based on the following two-steps splitting

$$i\partial_t \psi(\mathbf{x},t) = -\frac{1}{2}\Delta\psi(\mathbf{x},t) - \Omega L_{x_3}\psi(\mathbf{x},t), \quad (44)$$

$$\partial_t \psi(\mathbf{x},t) = V(\mathbf{x})\psi(\mathbf{x},t) + \beta|\psi(\mathbf{x},t)|^2\psi(\mathbf{x},t). \quad (45)$$

Then, the authors in [11] noticed that (44) can be split further as

$$i\partial_t \psi(\mathbf{x},t) = -\frac{1}{2}\partial_{x_1}^2\psi(\mathbf{x},t) - i\Omega x_2\partial_{x_1}\psi(\mathbf{x},t), \quad (46)$$

$$i\partial_t \psi(\mathbf{x},t) = -\frac{1}{2}\partial_{x_2}^2\psi(\mathbf{x},t) + i\Omega x_1\partial_{x_2}\psi(\mathbf{x},t). \quad (47)$$

The solutions of subsystems (45), (46) and (47) can be obtained by operators e^{tN}, e^{tX} and e^{tY} respectively, the second order BW method is then derived from the following composition

$$\begin{aligned}\psi^n(\mathbf{x}) &= \left(e^{\Delta t/2\,Y}e^{\Delta t/2\,X}e^{\Delta t\,N}e^{\Delta t/2\,X}e^{\Delta t/2\,Y}\right)^n\psi_0(\mathbf{x}),\\ &= e^{\Delta t/2\,Y}(e^{\Delta t/2\,X}e^{\Delta t\,N}e^{\Delta t/2\,X}e^{\Delta t\,Y})^{n-1}e^{\Delta t/2\,X}e^{\Delta t\,N}e^{\Delta t/2\,X}e^{\Delta t/2\,Y}\psi_0(\mathbf{x}).\end{aligned} \quad (48)$$

Combined with Fourier pseudo-spectral method in space, we can see that in each time step, we need six calls to FFT.

Lagrangian Method

Here we recall the main step of the method introduced in [10] to approximate (43). We will call it Lagrangian in the sequel. First, a change of coordinates is considered

$$\phi(\tilde{\mathbf{x}},t) := \psi(\mathbf{x},t) = \psi(e^{Jt}\mathbf{x},t),$$

where J is the 2×2 symplectic matrix. Then, ϕ satisfies the following equation

$$\partial_t\phi(\tilde{\mathbf{x}},t) = -\frac{1}{2}\Delta\phi(\tilde{\mathbf{x}},t) + W(\tilde{\mathbf{x}},t)\phi(\tilde{\mathbf{x}},t) + \beta|\phi(\tilde{\mathbf{x}},t)|^2\phi(\tilde{\mathbf{x}},t),\ \tilde{\mathbf{x}}\in\mathbb{R}^2, \quad (49)$$

with the initial condition $\phi(\tilde{\mathbf{x}},0) = \psi_0(\mathbf{x})$ and where W is defined by

$$W(\tilde{\mathbf{x}},t) = V(e^{Jt}\tilde{\mathbf{x}}),$$

so that a time dependency is created. However, if V is isotropic, $W(\tilde{\mathbf{x}}, t) = V(\tilde{\mathbf{x}})$ is time-independent. The main advantage of (49) does not involve the angular momentum rotation term and the following splitting is used

$$i\partial_t \phi(\tilde{\mathbf{x}}, t) = -\frac{1}{2}\Delta\phi(\tilde{\mathbf{x}}, t), \tag{50}$$

$$\partial_t \phi(\tilde{\mathbf{x}}, t) = W(\tilde{\mathbf{x}}, t)\phi(\tilde{\mathbf{x}}, t) + \beta|\phi(\tilde{\mathbf{x}}, t)|^2\phi(\tilde{\mathbf{x}}, t). \tag{51}$$

For harmonic potential V, each step can be solved exactly (which is not the case for general potential V). Combined with a Strang splitting and with Fourier pseudo-spectral method in space, we can see that in each time step, this method needs four calls to FFT.

3D Time-Periodic Quadratic Linear Schrödinger Equation

For (23) with $f = 0$ and B and V are specified in (32) and (33), we consider two numerical methods: ESQM and a standard Strang operator splitting.

Exact Splitting

The coefficients for ESQM (21) are given by

$$A_{\Delta t} \simeq \begin{pmatrix} 0.503369336514750 & 0.09260872887966 & -0.086577853155386 \\ 0.092608728879667 & 0.499175997238123 & 0.090475411725230 \\ -0.086577853155386 & 0.090475411725230 & 0.482430618251455 \end{pmatrix},$$

$$V_{\Delta t}^{(\ell)} \simeq \begin{pmatrix} 1.838313777101704 & 0 & 0 \\ 0 & 1.405233579215994 & 0 \\ 0 & 0 & 2.416160688906186 \end{pmatrix},$$

$$V_{\Delta t}^{(r)} \simeq \begin{pmatrix} 0.765638127548775 & 0.097739062052903 & -0.244124321719139 \\ 0.097739062052903 & 1.408683914880933 & 0.141925135897144 \\ -0.244124321719139 & 0.14192513589714 & 3.535113753227984 \end{pmatrix},$$

$$L_{\Delta t} \simeq \begin{pmatrix} 0 & 0 & 0 \\ 0.957867410476376 & 0 & 0 \\ -0.917880413070041 & 1.133563918623215 & 0 \end{pmatrix},$$

$$U_{\Delta t} \simeq \begin{pmatrix} 0 & -1.132325985517193 & 0.915677911046419 \\ 0 & 0 & -0.957661219232001 \\ 0 & 0 & 0 \end{pmatrix}.$$

Strang Method

Classically, we use the following operator splitting

$$i\frac{\partial\psi(\mathbf{x}, t)}{\partial t} = -\frac{1}{2}\Delta\psi(\mathbf{x}, t),$$

$$\frac{\partial\psi(\mathbf{x}, t)}{\partial t} = -(B\mathbf{x})\cdot\nabla\psi(\mathbf{x}, t),$$

$$i\frac{\partial\psi(\mathbf{x}, t)}{\partial t} = V(\mathbf{x})\psi(\mathbf{x}, t).$$

The solutions of the above three subsystems can be obtained by operators $e^{-it\frac{1}{2}\Delta}$, $e^{t\mathrm{Rot}}$, and $e^{-it\mathrm{V}}$ respectively so that we have the following second order splitting method

$$\psi^{n+1}(\mathbf{x}) = e^{-i\frac{\Delta t}{2}\mathrm{V}} e^{-i\Delta t\frac{1}{4}\Delta} e^{\Delta t\mathrm{Rot}} e^{-i\Delta t\frac{1}{4}\Delta} e^{-i\frac{\Delta t}{2}\mathrm{V}} \psi^{n}(\mathbf{x}). \tag{52}$$

Strang denotes (52) when $e^{\Delta t\mathrm{Rot}}$ is also approximated by a Strang directional splitting.

3D Magnetic Schrödinger Equation

From (35), where $\mathbf{A}(\mathbf{x}) = \mathbf{x} \times \mathbf{B}$, $\mathbf{B} = {}^{\mathrm{t}}(1, 0.1, 2)$ and V_{nq} is given by (36), we can use the following operator splitting

$$\begin{aligned}
i\frac{\partial \psi(\mathbf{x}, t)}{\partial t} &= -\frac{1}{2}\Delta\psi(\mathbf{x}, t),\\
\frac{\partial \psi(\mathbf{x}, t)}{\partial t} &= \mathbf{A}(\mathbf{x}) \cdot \nabla\psi(\mathbf{x}, t),\\
i\frac{\partial \psi(\mathbf{x}, t)}{\partial t} &= \frac{1}{2}|\mathbf{A}(\mathbf{x})|^2\psi(\mathbf{x}, t) + V_{nq}(\mathbf{x})\psi(\mathbf{x}, t),
\end{aligned}$$

The solutions of the above three subsystems can be obtained by operators $e^{-it\frac{1}{2}\Delta}$, $e^{t\mathrm{Rot}}$, and $e^{t\mathrm{VA}}$ respectively and we can derive a second order splitting method:

$$\psi^{n+1}(\mathbf{x}) = e^{\frac{\Delta t}{2}\mathrm{VA}} e^{-i\Delta t\frac{1}{4}\Delta} e^{\Delta t\mathrm{Rot}} e^{-i\Delta t\frac{1}{4}\Delta} e^{\frac{\Delta t}{2}\mathrm{VA}} \psi^{n}(\mathbf{x}). \tag{53}$$

ESR denotes the splitting method (53) when $e^{\Delta t\mathrm{Rot}}$ is solved by exact splittings for transport equation in Proposition 1. **Strang** denotes (53) when $e^{\Delta t\mathrm{Rot}}$ is approximated by Strang directional splitting.

The coefficients when $\Delta t = 0.1$ for ESQM (25) are as follows

$$A_{\Delta t} \simeq \begin{pmatrix} 0.506160069704187 & 0.098840554692409 & 0.001683128724191 \\ 0.098840554692409 & 0.508317718832811 & 0.050167780151672 \\ 0.001683128724191 & 0.050167780151672 & 0.501715861437068 \end{pmatrix},$$

$$V^{(\ell)}_{\Delta t} \simeq \begin{pmatrix} 2.025343613765655 & 0 & 0 \\ 0 & 0.508168767491105 & 0 \\ 0 & 0 & 0.000099459606977 \end{pmatrix},$$

$$V^{(r)}_{\Delta t} \simeq \begin{pmatrix} 0.072891278447532 & 0.242556937819776 & -1.026420948565178 \\ 0.242556937819776 & 1.959142247295385 & -0.046535665904951 \\ -1.026420948565178 & -0.046535665904951 & 0.508102737430800 \end{pmatrix},$$

$$L_{\Delta t} \simeq \begin{pmatrix} 0 & 0 & 0 \\ 2.003434507092443 & 0 & 0 \\ -0.099043028107977 & 1.016569585390557 & 0 \end{pmatrix},$$

$$U_{\Delta t} \simeq \begin{pmatrix} 0 & -1.963756896350695 & -0.099988990937417 \\ 0 & 0 & -1.006635420674690 \\ 0 & 0 & 0 \end{pmatrix}.$$

Proof of the Period 360

Lemma 1 *The function* $t \mapsto U_t = e^{it(\Delta/2 - V(x)) - tBx\cdot\nabla}$, *where* V *and* B *are given by* (32) *satisfies*

$$\forall t \in \mathbb{R},\ U_{t+180} = -U_t.$$

Proof Since $t \mapsto U_t$ is a group, we just have to prove that

$$U_{180} = -I_{L^2(\mathbb{R}^3)}.$$

We recall that by construction, we have $U_t = e^{-tq^w_{(\mathrm{QM})}}$ where

$$q^w_{(\mathrm{QM})} = i\frac{|\boldsymbol{\xi}|^2}{2} + iB\mathbf{x}\cdot\boldsymbol{\xi} + iV(\mathbf{x})$$

Step 1: To conjugate $q^w_{(\mathrm{QMS})}$ *to a sum of harmonic oscillators.* We are going to prove that there exists $V \in \mathcal{U}(L^2(\mathbb{R}^n))$ such that

$$U_t = V\exp(-it\sum_{j=1}^{3}\omega_j(x_j^2 - \partial_{x_j}^2))V^* \tag{54}$$

where $(\omega_1, \omega_2, \omega_3) = \frac{\pi}{180}(20, 75, 132)$. Assuming first this decomposition, we deduce that

$$U_{180} = V\exp(-20i\pi(x_1^2 - \partial_{x_1}^2))\exp(-75i\pi(x_2^2 - \partial_{x_2}^2))\exp(-132i\pi(x_3^2 - \partial_{x_3}^2))V^*.$$

But, in dimension 1, the eigenvalues of the harmonic oscillator $x^2 - \partial_x^2$ being the odd positive integers, we know that $\exp(i\pi(x^2 - \partial_x^2)) = -I_{L^2(\mathbb{R}^3)}$. Thus, we deduce that

$$U_{180} = VI_{L^2(\mathbb{R}^3)}(-I_{L^2(\mathbb{R}^3)})I_{L^2(\mathbb{R}^3)}V^* = -I_{L^2(\mathbb{R}^3)}.$$

In order to prove (54) we are going to apply the following theorem due to Hörmander.

Theorem 2 *(Hörmander, Theorem 21.5.3 in [27]) Let* $Q \in S^{++}_{2n}(\mathbb{R})$ *be a real symmetric positive matrix of size* $2n$. *There exists a real symplectic matrix* $P \in \mathrm{Sp}_{2n}(\mathbb{R})$ *of size* $2n$ *such that and some positive numbers* $\omega_1, \ldots, \omega_n$ *such that*

$$^tPQP = D(\omega)$$

where $D(\omega) = \mathrm{diag}(\omega_1, \ldots, \omega_n, \omega_1, \ldots, \omega_n)$ *is the diagonal matrix such that, for* $j = 1, \ldots, n$, $D(\omega)_{j,j} = D(\omega)_{j+n,j+n} = \omega_j$.

Indeed, here, it can be checked that $Q_{(\mathrm{QM})}$ (the matrix of $q_{(\mathrm{QM})}$) is a symmetric positive matrix (computing, for example, an approximation of its eigenvalues). Thus, applying Theorem 2, we get a symplectic matrix P and some positive numbers $\omega_1 < \omega_2 < \omega_3$ such that

$$^tPQ_{(\mathrm{QM})}P = D(\omega). \tag{55}$$

Consequently, since P is symplectic, we have

$$\exp(2tJQ_{(\mathrm{QM})}) = P\exp(2tJD(\omega))P^{-1},$$

where J is the symplectic matrix of $\mathbb{R}^{2n}$. Now, applying the monoid morphism (Theorem 3.1 in [12]) introduced also by Hörmander in [26], we get a function $t \mapsto \sigma_t \in \{\pm 1\}$ such that

$$\forall t \in \mathbb{R},\ U_t = e^{-itq^w_{(\mathrm{QM})}} = \sigma_t V \exp(-it \sum_{j=1}^{3} \omega_j (x_j^2 - \partial_{x_j}^2)) V^*$$

where $\pm V$ is the Fourier Integral Operator associated with P. Note that V is unitary. Furthermore, by a straighforward argument of continuity we deduce that $\sigma_t = 1$ for all $t \in \mathbb{R}$. Thus, to conclude, we just have to prove that $(\omega_1, \omega_2, \omega_3) = \frac{\pi}{180}(20, 75, 132)$.

Step 2: To determine ω. First, we observe that the matrices $JQ_{(\mathrm{QM})}$ and $JD(\omega)$ are similar. Indeed, since $P \in \mathrm{Sp}_6(\mathbb{R})$, we have ${}^tP \in \mathrm{Sp}_6(\mathbb{R})$ and applying (55) we deduce that

$$JD(\omega) = J\,{}^tPQ_{(\mathrm{QM})}P = (P^{-1}J\,{}^tP^{-1})\,{}^tPQ_{(\mathrm{QM})}P = P^{-1}JQ_{(\mathrm{QM})}P.$$

A fortiori, $JQ_{(\mathrm{QM})}$ and $JD(\omega)$ have the same eigenvalues. Thus, the eigenvalues of $JQ_{(\mathrm{QM})}$ are

$$\sigma(JQ_{(\mathrm{QM})}) = \sigma(JD(\omega)) = \{i\omega_1, -i\omega_1, i\omega_2, -i\omega_2, i\omega_3, -i\omega_3\}. \tag{56}$$

Consequently, to determine ω we just have to determine the roots of the characteristic polynomial of $JQ_{(\mathrm{QM})}$, denoted $\chi_{(\mathrm{QM})}$. By a straightforward calculation, we observe that

$$\left(\frac{3}{\pi}\right)^6 \chi_{(\mathrm{QM})}(\frac{\pi X}{3}) = X^6 + \frac{\lambda_1+\lambda_2+\lambda_3+3}{2}X^4 + \frac{\lambda_1\lambda_2+\lambda_1\lambda_3+\lambda_2\lambda_3+9/4}{4}X^2 - 3\frac{\lambda_1+\lambda_2+\lambda_3}{32} + \frac{\lambda_1\lambda_2+\lambda_1\lambda_3+\lambda_2\lambda_3}{8} - \frac{\lambda_1\lambda_2\lambda_3}{8}.$$

But, by construction $\lambda_1 < \lambda_2 < \lambda_3$ are the roots of the polynomial

$$7200X^3 - 72196X^2 + 222088X - 216341.$$

Thus, $\lambda_1+\lambda_2+\lambda_3$, $\lambda_1\lambda_2+\lambda_1\lambda_3+\lambda_2\lambda_3$ and $\lambda_1\lambda_2\lambda_3$ are some explicit rational numbers and we deduce that

$$\left(\frac{3}{\pi}\right)^6 \chi_{(\mathrm{QM})}(\frac{\pi X}{3}) = X^6 + \frac{407}{120}X^4 + \frac{123}{80}X^2 - \frac{7}{384}.$$

Finally, we verify by an explicit computation that

$$\chi_{(\mathrm{QM})}(i\frac{\pi}{9}) = \chi_{(\mathrm{QM})}(i\frac{5\pi}{12}) = \chi_{(\mathrm{QM})}(i\frac{11\pi}{15}) = 0.$$

So, we deduce of (56) that $(\omega_1, \omega_2, \omega_3) = \frac{\pi}{180}(20, 75, 132)$. □

References

1. Alphonse, P., Bernier, J.: Polar decomposition of semigroups generated by non-selfadjoint quadratic differential operators and regularizing effects. arXiv:1909.03662 (2019)
2. Ameres, J.: Splitting methods for Fourier spectral discretizations of the strongly magnetized Vlasov-Poisson and the Vlasov-Maxwell system. arXiv preprint arXiv:1907.05319 (2019)
3. Antoine, X., Bao, W., Besse, C.: Computational methods for the dynamics of the nonlinear Schrödinger/Gross-Pitaevskii equations. Comput. Phys. Commun. **184**(12), 2621–2633 (2013)
4. Antoine, X., Duboscq, R.: GPELab, a Matlab toolbox to solve Gross–Pitaevskii equations I: computation of stationary solutions. Comput. Phys. Commun. **185**(11), 2969–2991 (2014)

5. Antoine, X., Duboscq, R.: Gpelab, a matlab toolbox to solve Gross–Pitaevskii equations II: dynamics and stochastic simulations. Comput. Phys. Commun. **193**, 95–117 (2015)
6. Bader, P.: Fourier-splitting methods for the dynamics of rotating Bose–Einstein condensates. J. Comput. Appl. Math. **336**, 267–280 (2018)
7. Bader, P., Blanes, S.: Fourier methods for the perturbed harmonic oscillator in linear and nonlinear Schrödinger equations. Phys. Rev. E **83**(4), 046711 (2011)
8. Bader, P., Blanes, S., Casas, F.: Efficient time integration methods for Gross–Pitaevskii equations with rotation term. preprint arXiv:1910.12097 (2019)
9. Bao, W., Du, Q., Zhang, Y.: Dynamics of rotating Bose-Einstein condensates and its efficient and accurate numerical computation. SIAM J. Appl. Math. **66**(3), 758–786 (2006)
10. Bao, W., Marahrens, D., Tang, Q., Zhang, Y.: A simple and efficient numerical method for computing the dynamics of rotating Bose–Einstein condensates via rotating Lagrangian coordinates. SIAM J. Sci. Comput. **35**(6), A2671–A2695 (2013)
11. Bao, W., Wang, H.: An efficient and spectrally accurate numerical method for computing dynamics of rotating Bose–Einstein condensates. J. Comput. Phys. **217**(2), 612–626 (2006)
12. Bernier, J.: Exact splitting methods for semigroups generated by inhomogeneous quadratic differential operators. Preprint, arXiv:1912.13219 (2019)
13. Bernier, J., Casas, F., Crouseilles, N.: Splitting methods for rotations: application to Vlasov equations. SIAM J. Sci. Comput. **42**(2), 1 (2020)
14. Besse, C., Descombes, S., Dujardin, G., Lacroix-Violet, I.: Energy preserving methods for nonlinear Schrödinger equations. IMA J. Numer. Anal. **1**, drz067 (2020)
15. Besse, C., Dujardin, G., Lacroix-Violet, I.: High order exponential integrators for nonlinear Schrödinger equations with application to rotating Bose-Einstein condensates. SIAM J. Numer. Anal. **55**(3), 1387–1411 (2017)
16. Besse, N., Mehrenberger, M.: Convergence of classes of high-order semi-Lagrangian schemes for the Vlasov–Poisson system. Math. Comput. **77**(261), 93–123 (2008)
17. Caliari, M., Ostermann, A., Piazzola, C.: A splitting approach for the magnetic Schrödinger equation. J. Comput. Appl. Math. **316**, 74–85 (2017)
18. Chen, B., Kaufman, A.: 3D volume rotation using shear transformations. Graph. Models **62**(4), 308–322 (2000)
19. Coulaud, O., Sonnendrücker, E., Dillon, E., Bertrand, P.: J. Plasma Phys. **61**, 435–448 (1999)
20. Dujardin, G., Hérau, F., Lafitte, P.: Coercivity, hypocoercivity, exponential time decay and simulations for discrete Fokker–Planck equations. arXiv preprint arXiv:1802.02173 (2018)
21. Hairer, E., Lubich, C., Wanner, G.: Geometric numerical integration: Structure-Preserving Algorithms for Ordinary Differential Equations, Springer Series in Computational Mathematics (2006)
22. Hérau, F., Sjöstrand, J., Hitrik, M.: Tunnel effect for the Kramers-Fokker-Planck type operators: return to equilibrium and applications. Int. Math. Res. Not. **57**, 48 (2008)
23. Hérau, F., Sjöstrand, J., Hitrik, M.: Tunnel effect for the Kramers–Fokker–Planck type operators. Ann. Henri Poincaré **9**, 209–274 (2008)
24. Hérau, F., Thomann, L.: On global existence and trend to the equilibrium for the Vlasov–Poisson–Fokker–Planck system with exterior confining potential. J. Funct. Anal. **271**, 1301–1340 (2016)
25. Hochbruck, M., Ostermann, A.: Exponential integrators. Acta Numerica **19**, 209–286 (2010)
26. Hörmander, L.: Symplectic classification of quadratic forms, and general Mehler formulas. Math. Z. **219**, 413–449 (1995)
27. Hörmander, L.: The analysis of linear partial differential operators. III, classics in mathematics. Pseudo-differential operators. Springer, Berlin (2007). https://doi.org/10.1007/978-3-540-49938-1
28. Jin, S., Zhou, Z.: A semi-Lagrangian time splitting method for the Schrödinger equation with vector potentials. Commun. Inf. Syst. **13**(3), 247–289 (2013)
29. Li, Y., He, Y., Sun, Y., et al.: Solving the Vlasov–Maxwell equations using Hamiltonian splitting. J. Comput. Phys. **396**, 381–399 (2019)
30. McLachlan, R.I., Quispel, G.R.: Splitting methods. Acta Numerica **11**, 341–434 (2002)
31. Marsden, J.E., Ratiu, T.S.: Introduction to mechanics and symmetry: a basic exposition of classical mechanical systems. Springer, Berlin (2013)
32. Raymond, N.: Bound States of the Magnetic Schrödinger Operator. EMS Tracts Math. (2017)
33. Nicola, F., Rodino, L.: Global Pseudo-Differential Calculus on Euclidean Spaces. Birkhäuser, Basel (2010)
34. Welling, J.S., Eddy, W.F., Young, T.K.: Rotation of 3D volumes by Fourier-interpolated shears. Graph. Models **68**(4), 356–370 (2006)
35. Zeng, R., Zhang, Y.: Efficiently computing vortex lattices in rapid rotating Bose–Einstein condensates. Comput. Phys. Commun. **180**(6), 854–860 (2009)

Affiliations

Joackim Bernier[1,2,3] · Nicolas Crouseilles[4] · Yingzhe Li[5,6,7]

Nicolas Crouseilles
nicolas.crouseilles@inria.fr

Yingzhe Li
liyz@lsec.cc.ac.cn

1 Institut de Mathématiques de Toulouse, Toulouse, France

2 UMR5219, Université de Toulouse, Toulouse, France

3 CNRS, Université Paul Sabatier, 31062 Toulouse, Cedex 9, France

4 Univ Rennes, INRIA, MINGuS team, IRMAR - UMR 6625, 35042 Rennes, France

5 University of Chinese Academy of Sciences, Beijing 100049, China

6 LSEC, Academy of Mathematics and Systems Science, Chinese Academy of Sciences, Beijing 100190, China

7 INRIA, MINGuS team, Rennes, France